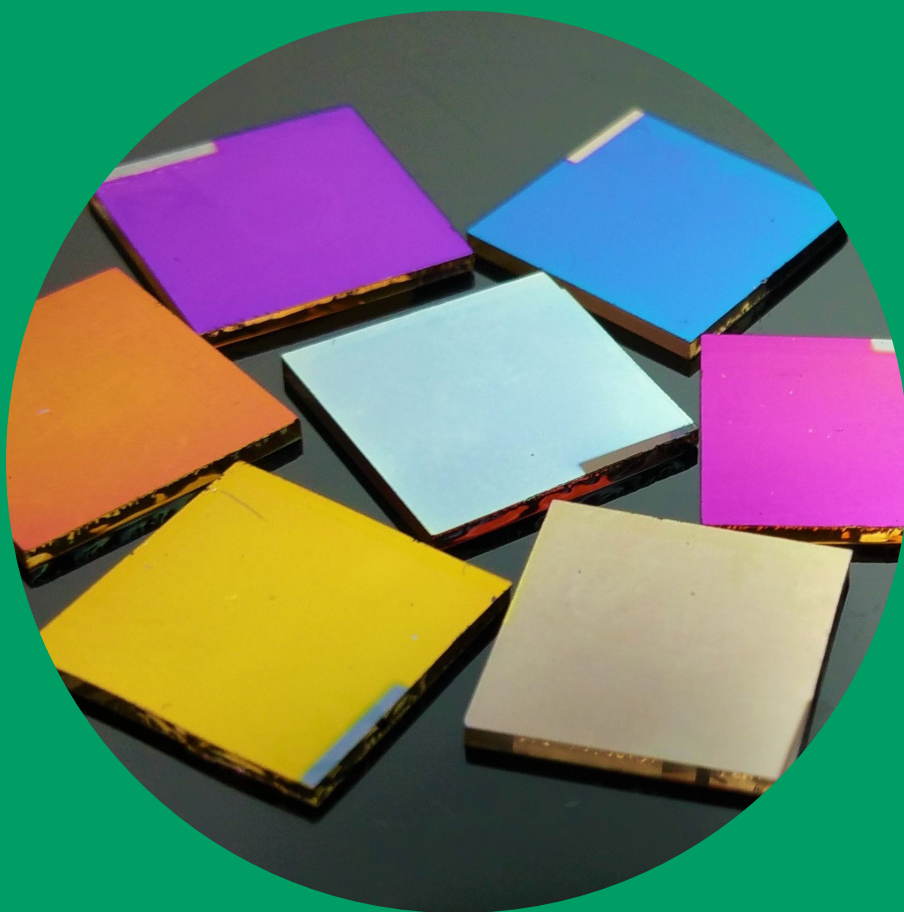


# Nanocomposite with Polarizonic Reflective Coloration: from Fabrication to Function

---

Moheb Abdelaziz



# Nanocomposite with Polarizonic Reflective Coloration: from Fabrication to Function

**Moheb Abdelaziz**

A doctoral dissertation completed for the degree of Doctor of Science (Technology) to be defended, with the permission of the Aalto University School of Chemical Engineering, at a public examination held at the lecture hall Ke5 of the school on 3rd December 2021 at 13:00.

Remote connection with Zoom:

<https://aalto.zoom.us/join/68760249450>

**Aalto University**  
**School of Chemical Engineering**  
**Department of Chemistry and Materials Science**  
**NanoChemistry and NanoEngineering**

**Supervising professor**

Professor Mady Elbahri, Department of Chemistry and Materials Science, Aalto University, Finland

**Thesis advisors**

Professor Franz Faupel, Institute for Material Science, Kiel University, Germany

Professor Jari Koskinen, Department of Chemistry and Materials Science, Aalto University, Finland

**Preliminary examiners**

Professor Paolo Milani, Department of Physics, University of Milan, Italy

Professor Andrey Shukurov, Department of Macromolecular Physics, Charles University, Czech Republic

**Opponent**

Professor Walter Remo Caseri, Department of Materials, ETH Zurich, Switzerland

Aalto University publication series

**DOCTORAL DISSERTATIONS** 160/2021

© 2021 Moheb Abdelaziz

ISBN 978-952-64-0595-7 (printed)

ISBN 978-952-64-0596-4 (pdf)

ISSN 1799-4934 (printed)

ISSN 1799-4942 (pdf)

<http://urn.fi/URN:ISBN:978-952-64-0596-4>

Unigrafia Oy

Helsinki 2021

Finland



**Author**  
Moheb Abdelaziz

**Name of the doctoral dissertation**  
Nanocomposite with Polarizonic Reflective Coloration: from Fabrication to Function

**Publisher** School of Chemical Engineering

**Unit** Department of Chemistry and Materials Science

**Series** Aalto University publication series DOCTORAL DISSERTATIONS 160/2021

**Field of research** Materials Science

**Manuscript submitted** 15 October 2021

**Date of the defence** 3 December 2021

**Permission for public defence granted (date)** 27 October 2021

**Language** English

☐ **Monograph**

☒ **Article dissertation**

☐ **Essay dissertation**

### Abstract

A sustainable future requires the exploitation of green and renewable energy sources such as an enhanced utilization of solar energy via solar absorbers. In this context, plasmonic nanostructures "nanodipoles" that are well-known for their unique absorption and scattering properties, have been previously introduced and explored by our group as perfect black solar absorbers. Such devices possess high efficiency when most of the visible spectrum is absorbed, hence dictating their fixed dark appearance. Nevertheless, such a dark appearance becomes aesthetically undesired from the decorative perspective. Herein, colored perfect solar absorbers with various vivid colors that originate from nanomaterials driven reflection rather than absorption is introduced. Such coloration results from a newly introduced phenomenon that was first reported by our group namely the polarizonic effect. In which disordered oscillating particles along with their cooperative interference action produce specular reflective colors "polarizonic reflective coloration" that has shown immense potential in a variety of advanced applications that are highlighted in this work. For instance the utilization of metallic nanoclusters and nanocomposites to design vividly colored perfect absorbers which can be tuned by engineering the polarizonic reflection resonance (PRR) via simply manipulating the filling factor, size, shape, and type of the nanoparticles in addition to the refractive index of the surrounding medium. Furthermore, flexible solar absorbers on aluminum kitchen foils showing vivid polarizonic reflection colors (PRCs) based on metallic nanocomposite are also presented. Additionally, a perfect solar absorber grounded on a new type of transfective "lossless" oxide metaparticles synthesized by Leidenfrost green nanochemistry is demonstrated. Finally, PRC and the Brewster Wavelength (BW) phenomena were employed as novel biosensors for both the naked eye and the biodetection of analytes even in a bulk state. Most of the films presented within this work were deposited via magnetron sputtering, which is a simple, cost-effective, scalable, and industrially established method.

**Keywords** Polarizonic, Plasmonic, Nanodipoles/Nanocomposite, Polarizonic reflection, Polarizonic reflection color(s), Brewster Wavelength (BW), Colored perfect absorber, Biosensing

**ISBN (printed)** 978-952-64-0595-7

**ISBN (pdf)** 978-952-64-0596-4

**ISSN (printed)** 1799-4934

**ISSN (pdf)** 1799-4942

**Location of publisher** Helsinki

**Location of printing** Helsinki **Year** 2021

**Pages** 102

**urn** <http://urn.fi/URN:ISBN:978-952-64-0596-4>





# Acknowledgment

Primarily, I would like to express my sincere appreciation and gratitude to my advisor and supervisor Prof. Dr.-Ing. Mady Elbahri, who has been a father, a brother, and a lifelong supporter. His incredible support, kind guidance, and extraordinary efforts were and will remain a great inspiration and motivation for me to push forward.

I would like also to express my great gratitude towards Professor Franz Faupel my first advisor who treated me as one of his group members, for his dedicated support on multiple occasions, valuable comments on the thesis, and allowing me to exploit his resources. I would also like to acknowledge Dipl.-Ing. Stefan Rehders, who designed the sputtering system, for his guidance concerning all the technical problems during these years and for sharing his knowledge in PVD systems. I also express my appreciation to Professor Carsten Rockstuhl for his valuable contribution to numerical analysis and simulation.

I want to express my sincere gratitude to my advisor Prof. Jari Koskinen for his support and valuable comments. I would like to acknowledge the help from Prof. Mehdi Hedayati, Adel Asaad, and Ahmed Soliman for their tireless efforts in revising this thesis.

Many thanks go to the members of the group both in TF Kiel, Germany, and at Aalto University, Finland, who provided me all the help and support I could ask for, among which are: Prof. Shahin Homaeigohar, Mehmet Yetik, Talha Munir, Dr. Dina Mosselhy, Dr. Usman Zillohu, Dr. Duygu Disci, and Dr. Eman Zarie.

A special thanks to my brother and colleague Dr. Ramzy Abdelaziz for his continued support, and encouragement.

A boundless appreciation to all my family members, my parents, my sisters, and my wife's parents for all the support, motivation, and prayers.

Yet, last not least, I am very thankful to my wife, Marwa Abdelrahman, and my daughters, Razan, Nuran, & Layan, for their continuous encouragement, motivation, and support.

Espoo, November 2021

A handwritten signature in black ink, reading "Mohab Abdelaziz". The signature is written in a cursive, flowing style with a long horizontal stroke at the end.



# Contents

Acknowledgment .....	i
List of Publications .....	v
Author's Contribution.....	vii
List of Abbreviations and Symbols.....	ix
<b>1. Introduction .....</b>	<b>1</b>
1.1 Plasmonic nanoparticles .....	1
1.2 Plasmonic nanocomposite.....	2
1.3 Plasmonic coloration .....	4
1.4 Plasmonic biosensing .....	5
1.5 Plasmonic metamaterial and energy saving .....	6
1.6 Polarizonic specular reflection: The concept .....	7
1.7 Research outline .....	11
<b>2. Materials and methods .....</b>	<b>13</b>
2.1 Materials .....	13
2.1.1 Targets .....	13
2.1.2 Substrates .....	13
2.2 Characterizations.....	14
2.2.1 UV-VIS spectroscopy.....	14
2.2.2 Spectroscopic Ellipsometer .....	14
2.2.3 Transmission Electron Microscope (TEM).....	15
2.2.4 Scanning electron microscopy (SEM).....	15
2.2.5 Grazing incidence X-ray Diffraction (GIXRD) .....	15
2.2.6 Profilometer.....	16
<b>3. Fabrication .....</b>	<b>17</b>
3.1 Sputter deposition technique .....	17
3.1.1 Sputtering chamber and magnetrons .....	19
3.1.2 Sample holder.....	21
3.1.3 Load lock chamber and sample transferring .....	22
3.1.4 Nano-composites, particles, and films fabrication .....	23
3.2 Leidenfrost technique.....	26
3.3 Spin-coating technique.....	27

<b>4.</b>	<b>Results and discussion.....</b>	<b>29</b>
4.1	Tailored perfect colored absorber (Publication 1) .....	29
4.2	Colored solar aluminum kitchen foils (Publication 3)....	32
4.3	Perfect black solar absorber (Publication 2).....	37
4.4	Naked-eye bulk biodetection (Publication 1).....	41
<b>5.</b>	<b>Conclusions .....</b>	<b>45</b>
<b>6.</b>	<b>Outlook.....</b>	<b>47</b>
	<b>References .....</b>	<b>49</b>
	<b>Publications .....</b>	<b>54</b>

# List of Publications

This doctoral dissertation consists of a summary and the following publications, which are referred to in the text by their numerals

**1.** Elbahri, Mady; **Abdelaziz, Moheb**; Homaeigohar, Shahin; Elsharawy, Abdou; Hedayati, MK; Röder, Christian; Assad, Mamdouh; and Abdelaziz, Ramzy; "Plasmonic Metaparticles on a Blackbody Create Vivid Reflective Colors for Naked-Eye Environmental and Clinical Biodetection." *Advanced Materials* 30 (2018): 1704442.

**2. Abdelaziz, Moheb**; Abdelaziz, Ramzy; Homaeigohar, Shahin; Zarie, Eman; Yetik, Mehmet; Sederholm, Linda; Liljeström, Touko; Peippo, Nella; Pflessner, Sebastian; Soliman, Ahmed; and Elbahri, Mady; "Transflective Mesoscopic Nanoparticles Synthesized in the Leidenfrost Droplet as Black Absorbers." *Advanced Materials Interfaces* 6 (2019): 1801610.

**3. Abdelaziz, Moheb**; Homaeigohar, Shahin; Hedayati, Mehdi; Assad, Mhd; and Elbahri, Mady; "Solar Aluminum Kitchen Foils with Omnidirectional Vivid Polarizonic Colors." *Advanced Optical Materials* 5 (2019): 1900737.



# Author's Contribution

**Publication 1:** Plasmonic Metaparticles on a Blackbody Create Vivid Reflective Colors for Naked-Eye Environmental and Clinical Biodetection

MA (the author) designed and performed most of the deposition experiments, prepared most of the samples, carried out most of the optical characterization, and contributed to the SEM characterization and the manuscript writing. SH contributed to the writing, editing, and revising of the manuscript. MKH and MEA contributed to the writing. AE and CR helped in designing the study from the biological point of view, selected the clinical samples, isolated and prepared extracellular vesicles & exosomes, and helped in writing the manuscript. MKH and RA took part in sample preparation and characterization. ME initiated the idea, conceived the concept, defined the research plan, supervised the work, and mainly wrote the manuscript.

**Publication 2:** Transflective Mesoscopic Nanoparticles Synthesized in the Leidenfrost Droplet as Black Absorbers

MA (the author) designed and performed most of the deposition experiments, prepared most of the samples, conducted most of the optical characterization, and wrote the first draft related to the optical properties under the supervision of ME. MA and RA mainly synthesized the materials (Leidenfrost oxide metaparticles) and performed the SEM characterization. SH contributed to the writing, editing, and revising of the manuscript. ESZ, MZY, LPS, TML, and NP, assisted in the synthesis of the materials. SP contributed to the sample fabrication. AS assisted in the synthesis of the materials and characterized the samples by XRD and analyzed the corresponding data. ME defined the research plan, conceived the concept, supervised the work, and finalized the manuscript writing.

**Publication 3:** Solar Aluminum Kitchen Foils with Omnidirectional Vivid Polarizonic Colors

MA (the author) designed and performed most of the deposition experiments, prepared most of the samples, performed most of the optical characterization, and cowrote the manuscript with ME. SH contributed to the writing, editing, and revising of the manuscript. MKH performed the simulation results. MKH and MAA contributed to the sample characterization. ME conceived the idea, defined the research plan, supervised the work, and finalized the manuscript writing.





# List of Abbreviations and Symbols

Ag	Silver
Al	Aluminum
AlN	Aluminum nitride
Au	Gold
Au NPs	Gold nanoparticles
BW	Brewster wavelength
BSA	Bovine serum albumin
Cu	Copper
CuO	Copper oxide
DC	Direct current
EBL	Electron beam lithography focused ion beam
FDTD	Finite difference time domain
FESEM	Field emission scanning electron microscopy
FIB	Focused ion beam
GIXRD	Grazing incidence X-ray diffraction
LSPR	Localized surface plasmon resonance
LSPRs	Localized surface plasmon resonances
NIR	Near infra infrared
NP	Nanoparticle
NPs	Nanoparticles
PRC	Polarizonic reflection color
PRCs	Polarizonic reflection colors
PRR	Polarizonic reflection resonance
PTFE	Polytetrafluoroethylene
PVA	Polyvinyl alcohol

PVD	Physical vapor deposition
RF	Radio frequency
RI	Refractive index
RI <sub>s</sub>	Refractive indices
SEM	Scanning electron microscope
Si	Silicon
SiO <sub>2</sub>	Silicon dioxide
SPR	Surface plasmon resonances
SPRs	Surface plasmon resonances
SPs	Surface plasmons
TEM	Transmission electron microscope
TiO <sub>2</sub>	Titanium dioxide
UHV	Ultra-high vacuum
UV	Ultraviolet
Vis	Visible
XRD	X-ray diffraction

A	Absorption
$a$	Radius of metal NP
B	Magnetic field
$d$	Nanoparticle's diameter
E	Electrical field
$e$	Charge of free electrons
F	Lorentz force
$f$	Filling factor
$f_{k0}$	Oscillator strength
$m$	Effective mass of electrons
$N$	Density of free electrons
$n$	Refractive index
$n_d$	Refractive index of the host medium
$P$	Static polarizability
$q$	Electron charge
R	Reflection
$S_R$	Biosensor sensitivity at reflection
V	Volume of metal NPs
$v$	Electron velocity
$\mathcal{E}_d$	Environment's dielectric constant
$\mathcal{E}_m$	Dielectric function of the metal
$\varepsilon_0$	Space's relative permittivity
$\mathcal{E}_1 + i\mathcal{E}_2$	Complex dielectric function of metal
$\varepsilon_\infty$	Dielectric function at a high-frequency range
$\omega$	Incident light frequency
$\omega_{k0}$	Eigenfrequency
$\omega_P$	Bulk plasma frequency
$\lambda$	Light's wavelength
$\lambda_{LSPR}$	The wavelength of the resonance peak
$\lambda_P$	Bulk plasma frequency's wavelength

$\delta_{k0}$	Damping constant
$\sigma_{ext}$	Extinction cross-section
$\alpha$	Dynamic polarizability
$\alpha_{res}$	Resonant dynamic polarizability
$\gamma$	Relaxation frequency
$\Delta\lambda$	Wavelength shift
$\Delta\lambda_s$	Wavelength shifts

# 1. Introduction

## 1.1 Plasmonic nanoparticles

Plasmonic metal nanoparticles (NPs) have been in use for thousands of years showing striking colors. These particles have resonant properties perceivable to the naked eye as color because of the fact that they absorb and scatter light at visible wavelengths[1]. The Lycurgus cup[2] manufactured in Roman times is considered a perceptible historical example proving the plasmonic coloration. The cup appears red and green with transmission and reflection modes, respectively. Both colors originate from gold-silver alloy NPs incorporated within a glass medium[2], [3], as shown in Figure (1a). As well known, metallic NPs can support surface plasmons (SPs) which are the collective oscillation of free conduction-band electrons localized at their surfaces. Thereby, these metal NPs “nanodipoles,” which possess dimensions in the quantum size regime, can strongly interact with the electromagnetic waves in a phenomenon known as “light-plasmon interaction.” At a specific frequency, called resonance frequency, this interaction generates a large enhancement of the localized electric field amplitude resulting from the coherent localized plasmon oscillations, known as localized surface plasmon resonances (LSPRs). The resonance state of a plasmonic nanodipole is illustrated in Figure (1b).

The Drude model described the behavior of the metal’s free electrons by the dielectric function  $\varepsilon_m$  that can be defined by equation (1)[4].

$$\varepsilon_m(\omega) = 1 - \frac{\omega_p^2}{\omega^2 + i\gamma\omega} \quad (1)$$

where  $\omega_p$ ,  $\omega$ , and  $\gamma$  are the bulk plasma, incident light, and relaxation frequencies, respectively. Whereas, the metal’s bulk plasma frequency is given by equation (2)[5].

$$\omega_p^2 = \frac{Ne^2}{\varepsilon_0 m} \quad (2)$$

where  $N$  is the density of conduction-band electrons,  $e$  their charge,  $\varepsilon_0$  expresses the space’s relative permittivity, and  $m$  act as the effective mass of electrons. For

real metals, the contribution of bound electrons, for example, inter-band transition that occurs at high-frequency range ( $\varepsilon_\infty$ ), needs to be added to the Drude model's equation (Eq. 1). Hence, the optical response of the electron of metal upon interacting with the light can be accurately calculated from equation (3).

$$\varepsilon_m(\omega) = \varepsilon_\infty - \frac{\omega_p^2}{\omega^2 + i\gamma\omega} \quad (3)$$

## 1.2 Plasmonic nanocomposite

Composite materials are fabricated from the incorporation of two or more dissimilar materials. Composite materials show a distinctive package of properties and functionalities not attainable by the individual constituent, particularly, when the NPs are used as a filler in the nanocomposites[6], [7]. In the last couple of decades, plasmonic nanocomposites have attracted the extensive interest of researchers as well as an industry due to their significant potential for peculiar optical applications[8]. The optical properties and resonant frequency of such nanocomposites are strongly influenced by the metal's composition, size, shape, distribution, filling factor, and surrounding medium. Nevertheless, the interaction between the local fields of the composite's nanoparticles should be also considered[9]. Figure (1c) shows the large enhancement of the local electric field at a hot spot near the nanoparticle's surface. As reported, the LSPR in plasmonic NPs is strongly affected by the presence of other neighboring NPs. For instance, at a narrow gap, a highly localized field arises from the plasmonic coupling (i.e., the coupling of LSPR modes of two neighboring NPs) via a near-field interacting[9], Figure (1d). The enhancement does not only depend on the interaction of local fields from different NPs but also can be strongly affected by the shape/morphology, distribution, and density of NPs[10]. As a result, in the case of a highly filled nanocomposite, microscopic, and macroscopic light confinement take place between the nanoparticles and within the hosting medium, respectively[8]. Such a microscopic local field can be controlled over the variation of interparticle spacing.

Concerning spherical metallic NPs that have a diameter much smaller than the incident light's wavelength, the electric field component seems like a uniform plane wave for the entire particle, in such a case retardation effects can be neglected. Thus, the interaction between light and the particle can be predicted using electrostatic approximation equations, rather than the electrodynamic (Maxwell's equations). The static polarizability ( $P$ ) of metal NP with radius ( $a$ ) which is quite smaller than the light's wavelength, is given by equation (4)[11] as follows:

$$P = 4\pi a^3 \frac{\varepsilon_m - \varepsilon_d}{\varepsilon_m + 2\varepsilon_d} \quad (4)$$

where  $\varepsilon_m$  and  $\varepsilon_d$  express the dielectric function of the metallic particle and hosted medium, respectively. When the denominator in (Eq. 4) is close to zero,

the polarizability reaches the maximum, resulting in the strongest optical response, also known as the Fröhlich condition[12].

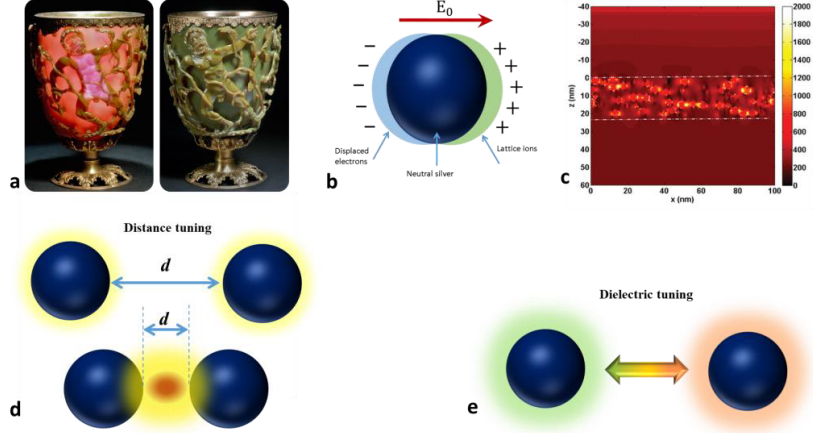


**Figure 1.** a) Lycurgus cup (4th century B.C) transmits a red light (a, left) and reflects green light (a, right) based on LSPR (re-modified from britishmuseum.com). b) Silver nanoparticle (10 nm-diameter) is illuminated with an electrical field of lightwave ( $E_0$ ), it follows that a displacement of electrons cloud compared to lattice ions resulting in electron density oscillation (localized surface plasmon, LSP) (re-drawn from Ref. [10]). c) FDTD simulation image of silver NPs immersed in silica medium when illuminated through resonance wavelength (430 nm), resulting in an enhanced local electric field at a hot spot (Reproduced Ref. [13]). d) Effect of changing of interspacing, resulting in near-field interacting “coupling” (d, bottom) at a small distance. e) Effect of change of the dielectric constant of the environment. d,e) Re-drawn from Ref. [8].

According to the Mie theory which is considered a simple method to explain the optical properties of spherical metallic NPs, the LSPR behavior can be described. For simplification, Mie established his theory for spherical particles with a diameter of  $d$  far less than the light’s wavelength  $\lambda$ , i.e., the ratio of  $d/\lambda \approx 0.1$ . Thus, the extinction cross-section  $\sigma_{ext}(\lambda)$  of the metallic NPs that is the sum of the scattering and absorption cross-sections, can be defined by equation (5):

$$\sigma_{ext}(\lambda) = \frac{18\pi V \epsilon_d^{3/2}}{\lambda} \frac{\epsilon_2(\lambda)}{[\epsilon_1(\lambda) + 2\epsilon_d]^2 + [\epsilon_2(\lambda)]^2} \quad (5)$$

where  $V$  is the nanoparticle volume,  $\epsilon_d$  acts the environment’s dielectric constant, and  $\epsilon_1 + i\epsilon_2$  expresses the complex dielectric function of the metal nanoparticle. When  $\epsilon_1$  equals  $-2\epsilon_d$  and  $\epsilon_2$  is a small value, the maximum size of  $\sigma_{ext}(\lambda)$  can be reached, that is the LSPR state. LSPR is extremely sensitive to any change in the environment’s dielectric constant, as shown in Figure (1e). The relationship between the wavelength of the resonance peak and the host medium’s dielectric constant can be calculated by equation (6):

$$\lambda_{LSPR} = \lambda_p \sqrt{2\epsilon_d + 1} \quad (6)$$



where  $\lambda_p$  is the bulk plasma frequency's wavelength. As a result, a redshift of the LSPR peak can be seen with an increment of the dielectric constant ( $\epsilon_d$ ) or refractive index ( $n_d$ ) of the host medium i.e.,  $\epsilon_d = n_d^2$ . [14]

Concerning the prediction of the optical properties of metallic nanocomposites with random size and shape distribution (certainly near percolation), not only Mie theory fails to predict the optical behavior of such composites but also the effective medium theories [15]. Such theories can work well for the simulation of composites with low filling factor [16] but fail to estimate the optical response of highly filled nanocomposites [17]. This is due to the dipole's interaction is not considered. Indeed, the nanocomposite's fascinating properties, such as a hot spot and a broadband resonance, etc., emerge when the volume fraction of embedded NPs is near the percolation threshold. In other words, Mie's theory fails to interpret the color observed in the luster pottery, Figure 2, which arises from the reflection and interference effects thus dictating that there is another phenomenon in play [15].

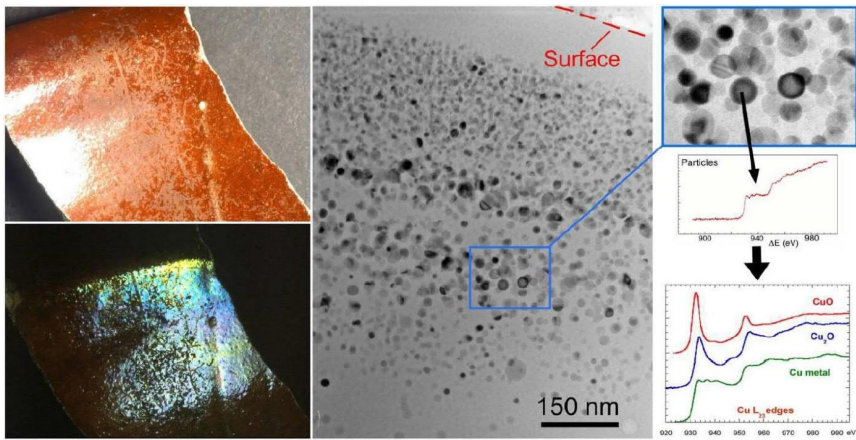


**Figure 2.** The 9th century CE lustered pottery belongs to Mesopotamia (Susa, Tunis). The color alters between red (top-left) and blue/green (bottom-left). TEM characterization displays the distribution mode of NPs (center and right). The graphs of EELS characterization show that the distributed NPs are fabricated of copper. © 2012 Sciau P. [18] under CC BY 3.0 license.

In the next sections, a brief overview of the literature is presented along with a discussion on the advanced applications of plasmonics such as structural coloration, biosensing, and energy harvesting while recognizing some of their limitations that have been resolved throughout the work of this thesis by using the new polarizonic concept.

### 1.3 Plasmonic coloration

When visible light hits a small object, reflective, scattered, transmitted, and absorbed light can be observed. So, this gives various information about this object, especially its “structural” color which is sensed with our eyes. The structural colors are the generation of colors from complex interference of sophisticated

nano/microstructures with visible light which can be seen in nature and daily life[19]–[21]. That is why these colors have attracted the interest of academia from a wide variety of fields[19], [22], [23]. In nature, structural colors can be observed among insects and birds[24]–[29]. Such colors arise from diffracted, scattered, and reflected light because of the interaction between light and the micro/nanostructure pattern of their skins/scales and wings[30]. Since then, researchers have paid attention and exerted effort to mimic these attractive colors of those creatures[31], [32]. Indeed, this kind of coloration method has significantly inspired the field of structural color printing based-plasmonic nanostructures i.e., plasmonic structural colors[33]. In principle, structural coloration is at most created from various optical processes such as thin-layer interference, diffraction grating, reflection grating, scattering of light, etc.[19]. Specifically, the coloration that is created through specular reflection and diffraction[34] of the light owns some features such as low energy consumption, eco-friendly, and high durability[20]. Such a way contrasts with the pigment colorants which are functioning by light absorption and scattering. Nevertheless, the majority of the plasmonic structural coloration is solely based on ordered nanoarrays fabricated through electron beam lithography (EBL), photolithography, or focused ion beam (FIB) techniques[30] which are costly and not suitable for upscaling. In addition, achieving such structural coloration using disordered particles and dipoles that can generate specular reflective vivid color has not introduced so far. Furthermore, the creation of controllable reflective coloration based on disordered metallic and semi-conductor dipoles with the sizes of a few nanometers has not been studied or considered until the present.

#### **1.4 Plasmonic biosensing**

The resonance of plasmonic nanosurfaces can show unique optical properties enabling the exploration/sensing of nanoscale environments. Additionally, the optical characterization of such produced samples can be done with conventional spectroscopic techniques. For this reason, the biosensing community paid high attention to the plasmonic field. In the last decades, sensors based on plasmonic structures showed great promise. Plasmonic biosensors can be divided into two classes of sensing platforms; the first type is film-based surface plasmon resonances (SPRs) sensing. In that one, SPRs excitation can arise along with flat or grating metal/dielectric interfaces. In the case of the flat metal film, the coupling between the light and the surface plasmon is achieved under the phase-matching condition by using, for instance, a prism with a refractive index (RI) greater than the analyte medium's RI[35]. The SPR biosensing is considered an interfacial sensing technique, therefore it can only detect a change in RI occurring near the film surface[36]. The other technique is the localized surface plasmon resonance (LSPR) biosensing of metallic NPs with dimensions smaller than the light wavelength enabling to confine the light to a small scale. Since LSPR possesses high sensitivity to RI changes in the surrounding medium, it can detect changes in molecular conformation and analysis of biomolecular

binding interactions[37], [38]. It is interesting to note that the LSPRs biosensing platforms have several advantages over SPRs ones. For example, LSPRs platforms are simple, amenable to miniaturization and multiplexing, and the tuning of LSPRs of the structures by varying the size, shape, etc., as well as can be excited directly by the light (no need for complex optics)[36]–[38]. Such biosensors as introduced in the literature can detect analytes just at a molecular level and within a few nanometers of the enhanced local field[39]–[43]. Thus, the LSPRs detection is not possible in the case of the variation of bulk refractive index (RI) as well as with a slight change of molecular polarizability. For that reason, bulk bio-detection based on plasmonic NPs is considered a huge challenge.

## 1.5 Plasmonic metamaterial and energy saving

Plasmonic metamaterials are artificially designed materials. Such materials are composed of dielectrics and noble nanometals enabling high optical state density in the nanoscale. This feature results from the coupling phenomenon between the surface plasmons in metal nanoparticles and photons.[44] Accordingly, this brings about fascinating properties e.g., light can be completely absorbed which are rare in raw or natural materials. The advantage of perfect absorptivity of light helped in the appearance of an emerging new generation of solar energy harvesting systems based-plasmonic materials. For instance, a solar perfect absorber structure with a total thickness of a few tens of nanometer was simply achieved by using plasmonic metallic nanocomposites that allow the light absorption in broadbands, tunable, and omnidirectional[45]. Such plasmonic nanocomposite composes of metal (e.g., gold, silver, and copper) nanoparticles with a high filling factor incorporated in a dielectric matrix such as SiO<sub>2</sub>, TiO<sub>2</sub>, and PTFE[46]. The metallic nanocomposites are formed of self-organized metallic nanostructures that disperse randomly in a dielectric material. This is due to the high cohesive energy of the metals and the interaction between metal and matrix. The nanocomposites are made by co-deposition via magnetron sputtering which is one of the physical vapor deposition (PVD) techniques. Thereby, the filling factor or fraction volume of metallic NPs can be easily controlled. The metallic nanostructures can be fabricated also based on electron beam lithography, but it is not attractive like PVD techniques. This is due to the ability of PVD to tailor the nanoparticles and their optical properties[44]. The low thickness of plasmonic metamaterial consequently its cost-effectiveness are making it applicable in photovoltaic devices or solar cells. A typical solar black absorber consists of three layers with a total thickness of 150 nm, top thin-layer based-metallic nanostructures, dielectric spacer (interlayer), and optically thick metal mirror[46], [47]. Moreover, a thin film based on plasmonic nanostructures[48] with a high filling factor (near the percolation) with a refractive index larger than the interlayer could give rise to a broad range of perfect absorption of light. Such absorptivity occurs in a wide range of spectrum from NIR and visible[46], [49], [50], down to ultraviolet[51] frequencies. In this context, a

broad range of light absorption was also achieved, but using a lithography fabrication technique[52], [53]. Moreover, absorption of light in a narrow band(s) was reported based on three layers of planar structures as well[54]–[57] using a periodic top layer of lithographic regular structures. The photonic community's interest is nowadays centered not only to produce and design perfect solar absorbers with dark coloration, in a simple, rational, and cost-effective manner but also generation of vivid colors. The tuning of such coloration in a simple (with no need for sophisticated lithographic techniques) and efficient way is still challenging.

## 1.6 Polarizonic specular reflection: The concept

All the research in the past and present concentrated significantly on the absorption and scattering of plasmonic nanostructures/nanocomposites while not considering their specular reflection. However, the specular reflection phenomenon could be significant, particularly concerning reflective coloration. As widely known, specular reflection has been commonly defined as the reflection of light from a smooth and mirror-like surface.[15] Such a phenomenon has been presented and explained as purely geometrical, while the illuminated matter enclosed has been ignored[15], [58]. The reflective coloration arising from disordered tiny plasmonic nanodipoles/nanocomposite that are well-known for weakly light scattering potential was studied and first introduced by this work's supervisor Prof. Elbahri during his Habilitation and presented in several articles[15], [59], [60] and adapted by other researchers[61], [62]. The plasmonic nano and molecular dipoles possess an electronic polarization what we call "polarizonic response," thus showing such specular reflection color at visible wavelengths, termed as polarizonic reflective color (PRC). This coloration can be seen due to the polarizonic reflection resonance (PRR) phenomenon that takes place when bounded dipoles oscillate at a specific wavelength, launching light waves into the far-field.

Indeed, in the case of the illumination of the nanodipoles (atom, molecule, or nanoparticle) by electromagnetic wave possessing wavelength much longer than dipole's diameter, the negative electron cloud will move relative to the positive ion core inside the dipole. In such a case, the electric field is considered homogenous, thus the quasi-static approximation can be applied. Owing to the attraction between these charges, the restoring force also exists, resulting in the charges oscillation "dipole oscillation". Such oscillation can be defined by Lorentz in the classical spring model, as shown in Figure 3a. The dipoles oscillate strongly and result in electro-dynamically coupled electric and magnetic fields, so radiating light away from the excited-objects. In that instance, the optical response of oscillating dipole should be explained by dynamic electronic polarization based on a complex dielectric function (Figure 3b), rather than the static one. Thus, the dynamic polarizability  $\alpha(\omega)$  can be described according to the spectroscopic conformity principle as follows:

$$\alpha(\omega) = \frac{e^2}{m} \sum_k \frac{f_{k0}}{\omega_{k0}^2 - \omega^2 - i\omega\delta_{k0}} \quad (7)$$

where  $\omega_{k0}$  is the eigenfrequency,  $f_{k0}$  acts the oscillator strength, and  $\delta_{k0}$  expresses the damping constant. If the frequency of the external field nears one of the eigenfrequencies of the transition oscillators so that the resonance condition ( $|\omega - \omega_{k0}| \leq \delta_{k0}$ ) is achieved and one resonant summand in the sum (Eq. 7) is kept, the dynamic polarizability at resonance state  $\alpha_{res}(\omega)$  can be estimated from equation (8).[15], [63]

$$\alpha_{res}(\omega) = \left( \frac{e^2}{2m\omega_{k0}} \right) \frac{f_{n0}}{\omega_{k0} - \omega - \frac{i\delta_{k0}}{2}} \quad (8)$$

Based on that, the resonant polarizability consists of real and imaginary components. The real one acts the electromagnetic wave's reflection & refraction and can be positive for dielectrics and molecules or negative for metals. Whereas the imaginary component signifies the radiation's absorption. Therefore, the absorption and specular reflection processes occur at the resonance wavelength.[15], [63] The complex refractive index (RI) is a representation of the system's complex dielectric function, thus plays a prominent part in the optical properties of the nanocomposite system.

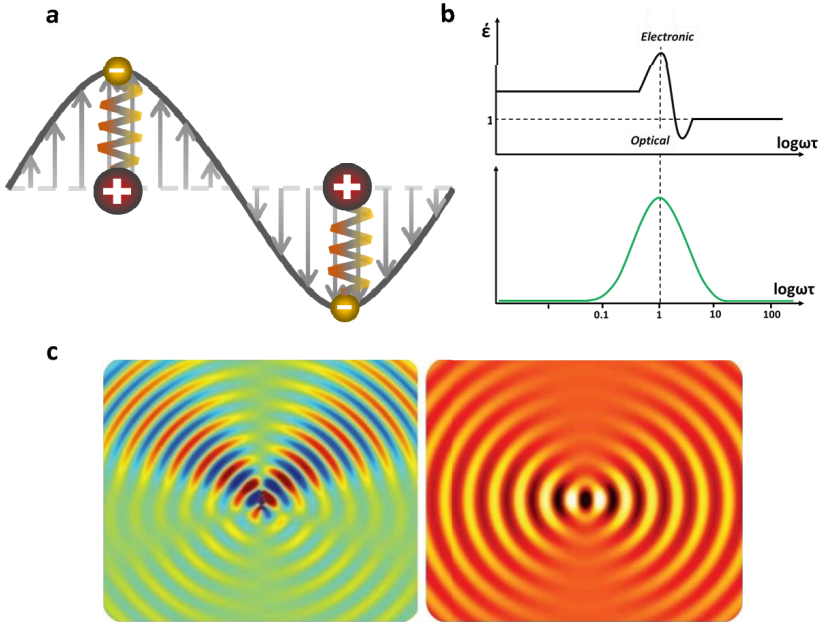


**Figure 3.** a) Schematic shows an oscillating electric field moving dipole's charges relative to each other (Re-drawn from Ref. [59]). b) Variation of the dielectric function against the frequency indicating electronic polarization (Re-drawn from Ref. [15]). c) The left Image simulates the interference and directed light radiation of six dipoles nearby proximity; the right image shows the Hertzian electric dipole antennas localize the electrical current and thereby radiate an electric field, Reproduced from Ref. [64].

Indeed, specular reflection of oscillated dipoles is a cooperative process. The oscillation of dipoles happens in a collective manner causing a cooperative dipolar coupling. In other words, the superposition of the induced waves of the individual excited dipoles results in a coherent cooperative coupling which causes radiating electromagnetic waves in far-field “resonating specular reflection.” As shown in Figure 3c (left), when several Hertzian dipoles find close to each other, the interaction of their local field radiation patterns gives rise to a dipolar photonic event. In such a case, the cooperative dipolar coupling results in macroscopic radiation modes that are spatially and temporally coherent and differ strongly from the modes of an individual dipole. Eventually, these radiation modes appear as a specular reflection. In contrast, a single dipole oscillator is not able to create such modes, thus the reflection cannot be seen by a single dipole oscillator, as illustrated in Figure 3c (right).[13], [15], [64], [65] Based on this idea, we have presented experimental proof of specular reflection created by disordered plasmonic nanodipoles/nanocomposite at visible frequencies.

The plasmonic nanodipoles with diameters of less than 10 nm are famous for their strong absorptivity[66], [67]. However, in this work, we showed that the PRC can be readily created by randomly distributed plasmonic nanostructures on a surface either standalone, embedded, or covered by a host medium. It has been proven that such structures (i.e., no need for a special arrangement) perform as macroscopic antennas and conduct as nanomirrors. Therefore, these structures can generate polarizonic reflective coloration at the resonance wavelength even if it exists on a black substrate, as shown in Figure 4, and experimentally demonstrated (chapter 4).

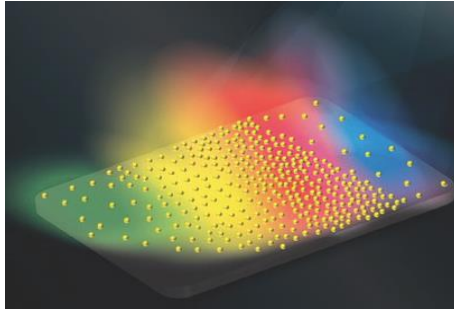


**Figure 4.** Schematic view of polarizonic reflection colors generation from the plasmonic nanoparticles deposited on a blackbody with different filling factors. Reproduced with permission[64].

As reported, both polarizonic specular reflection and plasmonic absorption happens at an identical resonance frequency. Thus, the polarizonic resonance (i.e., reflection coloration) can be adjusted via the common plasmonic parameters, such as nanoparticle’s size, filling factor, medium refractive index, and the type of dipole. Once one or more of these parameters varies, the effective medium’s refractive index (RI) of the nanocomposite is altered. When the real part of complex RI is dominant, the polarizonic specular reflection takes place, consequently appearance vivid PRC.[60]

In this thesis, the tailoring of surface optical behavior in terms of the polarizonic reflection response thus creating polarizonic structural coloration can be realized. In this regard, the metallic nanostructures are utilized for the design of a tailored perfect-colored absorber via changing the type of the nanometals, their volume fraction, and hosting medium. We show that the polarizonic resonance can be adjusted by combining two different dielectric matrices such as  $\text{TiO}_2$ ,  $\text{SiO}_2$ , and  $\text{AlN}$  thus covering a broad range of frequencies. Moreover, the metallic nanocomposites, as well as metacomposites fabricated based on trans-flective oxide particles such as  $\text{CuO/PVA}$ , were utilized with optically thick metal films. The use of such a combination (i.e., composite/metal film) offers perfect light trapping owing to the polarizonic reflection interference, thus can be used to convert a thin-film solar absorber material into any color including black. On another hand, the ability of the plasmonic nanoparticles system to attain high environmental detection based on polarizonic phenomenon was introduced in the biosensing area. Such detectability relating to the host medium is owing to the reliance of polarizonic reflection on the propagation delay, i.e., the RI's real part. In this respect, the Au-NPs template based on polarizonic reflection and Plasmonic Brewster Wavelength (BW) effect[20] is presented as a new base for naked-eye and bulk detection of biological analytes.

Conclusively, polarizonic reflection coloration can be defined as a color caused by a propagating wave that arises from the cooperative dipolar coupling of polarized materials that include not only metal but metal oxide as well. Through this concept, some striking properties that are not achievable via the plasmonic extinction can be accomplished. Thereby, this concept can open a new way of using such disordered dipoles in structural coloration, energy-saving, and biomedicine fields, as explained in chapter 4.

## 1.7 Research outline

In this dissertation, polarizonic reflective colored nanostructures were deployed to tackle the abovementioned limitations (mentioned in sections 1.3, 1.4, and 1.5) in terms of energy harvesting, biosensing and structural coloration. For instance, the polarizonic reflective nanostructures/nanocomposites which are produced by sputtering or Leidenfrost reactor were utilized to fabricate tailored perfect-colored absorber. Additionally, Brewster Wavelength (BW) phenomenon was employed as a new base for the naked-eye and biodetection of analytes even in a bulk state. In this regard, the applications presented in this work are illustrated as follows (Figure 5):

- The design of colored perfect absorbers based on metallic nanoclusters[64] (Publication 1).
- The design of biosensors enabling naked-eye and bulk analyte detection[64] (Publication 1).
- The design of flexible solar aluminum kitchen foils in attractive polarizonic colors[13] (Publication 3).
- The design of a perfect solar absorber based on Leidenfrost transfective oxide metaparticles[65] (Publication 2).

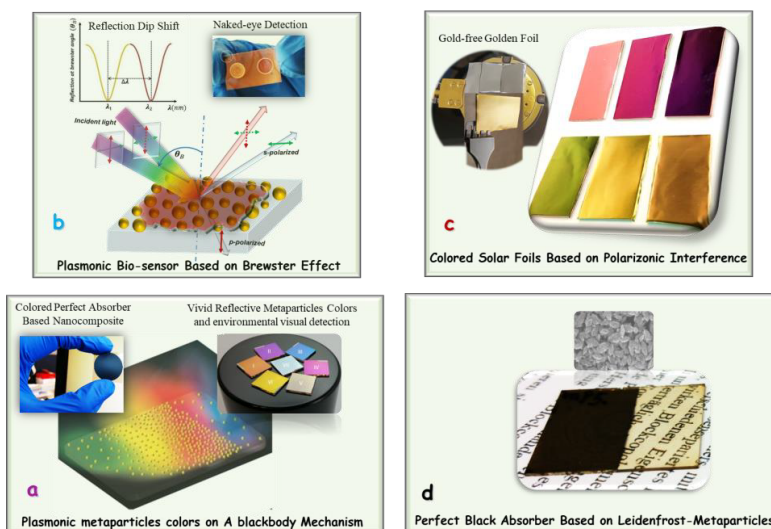


**Figure 5.** Schematic illustration of the possible applications of polarizonic reflection and the BW effect of disordered particles/nanocomposite.





## 2. Materials and methods

During my PhD work, various materials including sputtering targets, a custom-made magnetron sputtering machine, and characterization instruments were utilized. In this chapter, the specifications of these materials and instruments are briefly presented. Whereas the magnetron sputtering system that is considered the core of my PhD work for preparing the samples is fully explained in detail in section 3.

### 2.1 Materials

For preparing the CuO metaparticles, the precursor aqueous solution was prepared from copper (II) acetate (purity 99.99 % Sigma Aldrich). Polyvinyl alcohol PVA dissolved in water was used to be a hosting medium of the CuO particles dispersed in water resulting in the forming of CuO/PVA metacomposite. The thin film coatings based on the metacomposite (CuO/PVA) were prepared via spin-coating technique (discussed in section 3.3).

#### 2.1.1 Targets

In this dissertation, the used metal and dielectric sputtering targets were provided by FHR Anlagenbau Co. with 51mm diameter and utilized without any further modification. The metallic targets were gold and silver with 99.99% purity. Moreover, the metal's thicknesses were 2 mm for Au with a copper backing plate of 4mm and 6mm (without backing plate) for Ag. On another hand, the dielectric targets (SiO<sub>2</sub>, TiO<sub>2</sub>, and AlN) were used with 99.99% purity. Whereas the thickness of each one was 4mm with around 2 mm copper backing plate.

#### 2.1.2 Substrates

A glass, silicon, and kitchen aluminum (Al) foil were used as substrates. All the substrates were cut into sizes considering the sample holder head (the plasma covered area). The glass substrate with the following dimensions: 76\*26\*1 mm and 20\*20\*0.5 mm (Thermo SCIENTIFIC (MENZEL-GLÄSER), EYDAM Co.) were used. Whereas, the silicon substrates (wafers) were provided by Si-Mat Co., with the following specifications: 525 mm wafer's thickness, one side polishing, the resistivity of around 10 ohms.cm, and n-doped type. The flexible Al foil can be ordered with a thickness of around 0.02 mm from the common supermarkets. The Al foil particularly in metallic bright colors has been utilized for decoration, packaging, and art. Moreover, due to its best surface reflectivity,

high strength, lightweight, and excellent electrical and thermal conductivities, it can be used in energy applications including industrial solar material[13].

## 2.2 Characterizations

### 2.2.1 UV-VIS spectroscopy

Some of the samples were optically characterized by unpolarized light by UV/Vis/NIR spectrometer (PERKIN ELMER, Lambda 900) for measuring specular reflection spectra. This instrument has two light sources (Deuterium and Halogen lamps) allowing the measurement over a spectral range from 190nm to 3300nm. For specular reflection measurement (@6degree) all the samples were measured against Al-mirror as a reflection standard. Moreover, for monitoring the measurements and data manipulation, the instrument can be connected to a PC supported by software (UV WinLab) made by PerkinElmer company. Regarding the baseline measurement, the machine scans the reference mirror twice under the selected wavelength range. Whereas, in the case of the real sample measurement, the machine scans one time. The scan step value was selected 4nm for all measurements. When the transmittance of the prepared samples equals zero, the absorption spectra can be determined from this equation:

$$1 - R(\lambda) = A(\lambda) \quad (9)$$

### 2.2.2 Spectroscopic Ellipsometer

The optical properties including reflection and transmission spectra of the fabricated samples were carried out with polarized light by the ellipsometer from J.A. Woollam Co., Inc. as illustrated in Figure 6. The specular reflectivity spectra with angle variation from 45° to 85° of incidence with a selected angle step 5 or 10 were done. By applying a specific model, the optical constants and the film thickness can be determined. Such a device has dual light sources (Deuterium and Quartz Tungsten Halogen (QTH) bulbs), thus the optical measurements can be achieved with a spectral range from the UV to the NIR region (245nm to 1687nm). For data acquisition e.g., analyzing and monitoring, the instrument was connected to a PC supported by CompleteEASE software made by J.A. Woollam company. Since the polarization state of the light can be affected by the sample reflection, the p and s-polarized reflectivity spectra of the sample were achieved in various oblique incident angles. Concerning the measurement of the sample reflection, the machine should be calibrated initially by baseline measurement. This occurs by a silicon wafer coated with thermal oxide (SiO<sub>2</sub>) which works as a reference sample. On the other hand, for transmission measurement, the baseline data should be collected by measuring a reference sample (such as air or naked glass).



**Figure 6.** Camera Image of the ellipsometer device from J.A. Woollam Co., Inc.

### **2.2.3 Transmission Electron Microscope (TEM)**

In this work, the samples containing nanocomposite or nanoclusters were characterized using TEM (FEI/Philips Tecnai F30 G2) giving high-resolution images (with a resolution of 0.1 nm) with valuable information about the distribution, the size, and the shape of nanoparticles. For the samples which were done at room temperature, commercial copper TEM grids were used, while, for the ones prepared at elevated temperature, nickel TEM grids were utilized. Since the resolution is influenced by the thickness of the specimen, the ultra-thin film is preferable. For this aim, the nanocomposite sample was prepared with 20nm thick, thereby high-resolution images can be taken.

### **2.2.4 Scanning electron microscopy (SEM)**

Size distribution and surface morphology of the oxides and metal nanostructures samples synthesized by Leidenfrost reactor and sputtering technique, respectively, were investigated by SEM (Phillips XL 30 and Field Emission SEM, ZEISS ULTRA PLUS). The material surface imaging is achieved with the SEM through a highly energetic focused electrons beam. The beam is accelerated at a voltage range from 0.5 to 30 kV. Whereas, in field emission scanning electron microscopy (FESEM), the primary electrons are generated by field emission electron source. Thus, high-resolution images showing clearly surface information of the sample can be easily attainable. In this work, the samples of oxide powder (CuO with different morphology) and silver & gold NPs (sputtered at elevated temperature) were prepared on silicon wafers to be characterized.

### **2.2.5 Grazing incidence X-ray Diffraction (GIXRD)**

In basic X-ray diffraction (XRD), the incoming beam travels with large incident angles, penetrates deep into a crystalline material (sample). XRD is a non-destructive analytical tool that can characterize crystalline materials and determine their physical properties and chemical compositions. Bragg's law is used to explain, how constructive interference occurs from atomic planes, thereby diffraction/reflection peak can be recognized. Here, GIXRD in which the amount of X-ray reflection from the thin layer would be maximized compared to the strong signal from the substrate was used. In such a technique, the X-ray

beam hits onto the sample's surface at a small incident angle (1 or less) below the critical angle, consequently, the diffraction ray from lattice planes can be collected by a specific detector. In this thesis, the crystallinity and composition of the fabricated oxide metaparticles (CuO with different morphology) were analyzed by the GIXRD technique worked by a Panalytical X'Pert diffractometer using parallel beam optics. The characterizations were done at ambient temperature and Cu-K $\alpha$  radiation (wavelength = 1.5418 Å) at 40 kV and 40 mA.

### **2.2.6 Profilometer**

A profilometer device is commonly utilized for the measurement of thickness and surface roughness as well. The sample surface height variation can be determined in the used Stylus profilometer (Bruker Dektak XT) via sensing a fine stylus deviation moving across the surface. For the thickness measurements, a glass substrate coated with a metallic thin film e.g., gold having extremely poor adhesion was prepared. Subsequently, the film can be mechanically scratched by a very sharp tweezer for removing some film narrow tapes without the glass being scratched. In contrast to metals, dielectric films (e.g., TiO<sub>2</sub>) have great adhesion making the scratching is useless for measuring the thickness. Hence, to be able to measure the thickness, a part of the glass substrate should be covered with a very narrow band of aluminum foil. By removing the aluminum foil, the thickness depth can be measured between coated and uncoated areas (covered with Al foil). However, the thickness value which was measured is not accurate hundred percent because of the shadow effect caused by the aluminum edge. In that case, the dielectric thickness can be measured by an ellipsometer (with a suitable model) to confirm the measured value accuracy. In that way, a good matching between ellipsometer measurement and profilometer one should be shown.

### 3. Fabrication

So far plasmonic nanocomposites have been mostly fabricated based on two dissimilar materials (e.g., metal NPs embedded in dielectric hosting medium). The plasmonic/polarizonic resonance peaks of such composites strongly depend on the type of the nanometals and the surrounding dielectric matrix. The limited number of dielectric materials and their corresponding refractive indices raise a challenge to freely tune the resonance band in a broad range of wavelengths. Thus, to address this challenge a custom-made three-source magnetron sputtering system was fabricated. The design and assembly processes of the system as well as the preliminary running until achieving satisfactory results took more than two years. Such a system permits the deposition of three different materials simultaneously, e.g., two dielectrics and one metal, thus the resonance can be tuned by developing a hybrid dielectric composite. The refractive index of this hybrid dielectric can be adjusted by varying the ratio of the components instead of altering the material of the matrix. This fabrication method enables a spectrum of novel nanocomposite materials that can be applied in a variety of advanced applications such as energy-saving and structural coloration.

#### 3.1 Sputter deposition technique

The sputtering process-based inert gas discharge can be achieved by surface atoms ejection from the target (cathode) under bombardment with positive gas (usually argon) ions. Based on the connected power supply applied across the anode and cathode, the sputtering process can be categorized into DC or RF sputtering (diode sputtering). At most, the conductive materials deposition is performed by DC sputtering. Whereas RF sputtering is needed for depositing insulating materials. However, there are some problems in diode sputtering systems such as lower deposition rate, higher substrate temperature (due to secondary electrons), and higher gas pressure. From then, the magnetron sputter system which is a low-pressure sputtering technique was introduced to overcome these drawbacks. In such a system, the plasma is concentrated by the secondary electrons confinement within a region about the target. This occurs by placing permanent magnet pieces behind the target material. It is worthy to note that the magnetron sources in the sputter system are utilized in 95% of all sputtering applications[68].

The planar magnetron is one of the commonly used magnetrons types for thin film deposition. A schematic view of the used planar magnetron is illustrated in Figure 7. In the presence of the magnetic field (B) lines caused by the magnet

pieces in the area locating directly over the target as well as an electrical field (E) of the applied voltage across the target and anode shield, the electrons in gas discharge are influenced by electromagnetic force, called Lorentz force (F) therefore following a spiral path.

$$F = -q(E + v \times B) \quad (10)$$

where  $q$  is the electron charge,  $v$  is the electron velocity. As a result, the electron path length becomes much longer, thereby enhancing the argon atom's ionization efficiency. Consequently, this creates high-density plasma at a much lower pressure gas compared to classical diode sputtering. The target is eroded under the electron closed path causing an etch track.

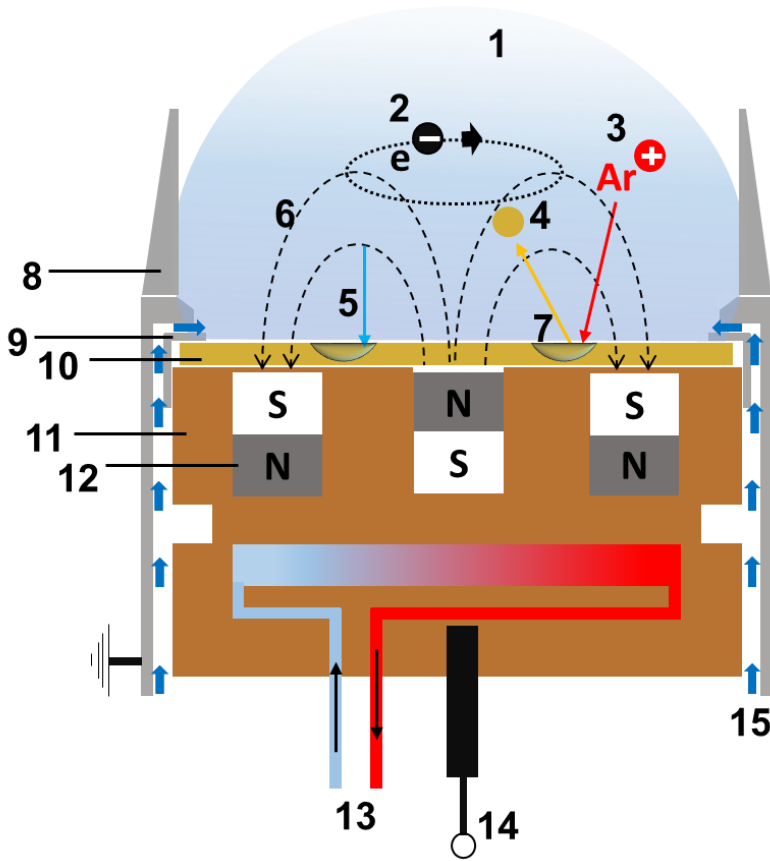


**Figure 7.** Schematic diagram of the used planar magnetron showing the principle of the sputtering process, glow discharge (plasma) (1), electron spiral track (2), Argon positive ion (3), target atom (4), electric field (5), magnetic field (6), erosion area (7), chimney (anode shield) (8), target clamp (9), target (10), copper body (11), magnet piece (12), cooling water (13), a negative HV & RF potential (cathode) (14) and gas (Ar) inlet (15).

The used magnetron sputtering machine in this work is designed (by Stefan Rehders, Kiel) and assembled in the house as illustrated in Figure 8. The system

consists of four main parts: a main chamber for the sputtering process, load lock chamber & transfer system, cooling system, and powering & controlling unit. Moreover, the main chamber and load lock chamber can be separated with a UHV gate valve. Such a feature allows fast sample entry and provides the system flexibility to place samples with keeping the vacuum level of the deposition chamber. In the following, the functions of these parts are described in more detail.



**Figure 8.** Camera Image of the sputtering system consisting of a deposition chamber (a), a load lock chamber (b), a cooling system (c), and a powering & controlling unit (d).

Our sputtering system has three magnetrons, each one includes a specific target with a diameter of 51 mm and is fixed on a ConFlat (CF) flange. Whereas the distance between the substrate and target can be attuned by magnetron height altering. Moreover, the sputtering chamber was built in a way that allows using a large variety of materials, e.g., metals and dielectric oxides. It also allows the deposition of three materials (co-sputtering) simultaneously.

### 3.1.1 Sputtering chamber and magnetrons

The schematic of the sputtering cylindrical chamber is shown in Figure 9. At the ends of this cylindrical chamber, there are two large DN250 CF flanges. One of them works as a flat entry lock door, while the second one is used to fix the sample holder. Moreover, there are many flanges of varied sizes distributed in the chamber's surroundings. This allows a vast variety of geometric configurations and sputtering processes. The sputtering chamber is pumped down to a pressure range of 10<sup>-8</sup> mbar by a multistage root dry pump (Pfeiffer ACP-28) and a turbomolecular pump (Pfeiffer HiPace 300). Both are controlled over the tur-



bomolecular pump's controller. Accordingly, they can start and stop simultaneously by switching on/off the turbomolecular pump. The deposition chamber venting is achieved by the turbomolecular pump's controller through nitrogen gas injection. Besides, a multi-gas controller (MKS 647C gas flow system) controls the chamber argon inlet through three mass flow valves.

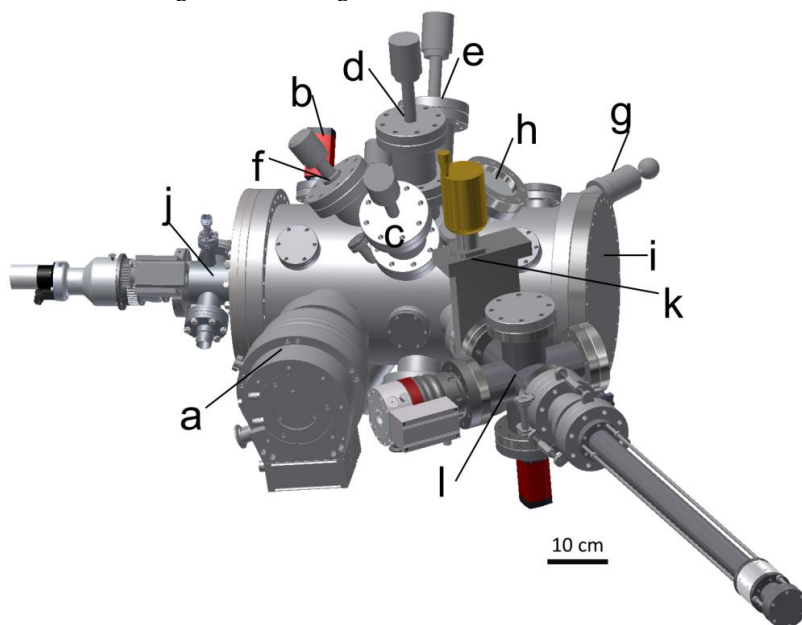


**Figure 9.** The geometry of the deposition chamber included a turbomolecular pump (a), pressure gauge (b), three magnetrons (c,d,e), rotary shutter (f), main shutter(g), glass window (h), lock door flange (i), sample holder (j), a UHV gate valve (k) for the load lock and sputtering chambers separation, and load lock chamber (l).

The magnetrons (PLANARMAGNETRON\_ION´X-2UHV\_9254) are built by Thin Film Consulting Co., to be fit with the disc sputtering target with 51mm diameter and 1 to 6mm thickness. They are fixed on a DN63 CF flange. The magnetron can be powered by a DC power supply (MDX 500) or an RF power generator (CESAR\_600 WRF) combined with a matching network box. The type of connected power supply depends on the sputtering material e.g., metal, or dielectric.

A chiller unit is necessary for heat removal from the target to cooling water which is ensured by the interlock system. Nevertheless, the dielectric targets which have a low thermal conductivity should be used with copper backing plates of 2 to 4mm thickness.

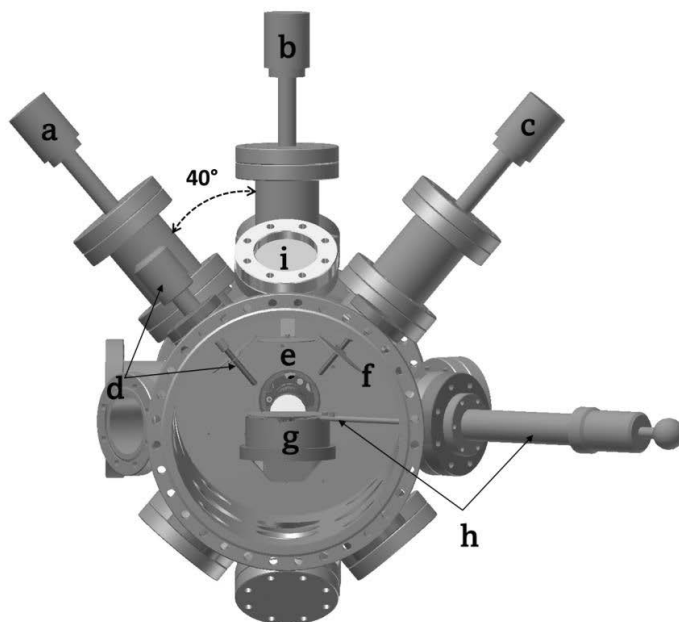


**Figure 10.** Schematic view of the sputtering cylinder chamber showing three magnetrons (a,b,c where the magnetron (a) makes 80° with magnetron (c)) with their rotary shutters (d with its hand,e, and f) respectively, sample holder base (g) covered with a linear shutter (h), and glass window (i).

To be able to adjust plasma parameters and keep the substrate in a clean state, it should be covered completely by the linear shutter in a non-tilted mode as shown in Figure 10. Also, the three individual rotary shutters can move around the magnetrons' chimneys. Such shutters can prevent the targets of magnetrons that are not used from being contaminated because of an active one.

### 3.1.2 Sample holder

The sample holder, as shown in Figure 11, is used as a seat for the samples with multiple features that allow heating up, rotation, and tilting of the sample base. It is fixed on a large DN250 CF flange. The heating up of the sample is provided by Pyrolytic graphite coated Graphite heating (PgG) element up to 1000 C°. It is powered by a power supply (SM70-AR-24) via an MS-style connector. Moreover, the measurement and reading of the temperature occur via a type K thermocouple and monitor device (Digital thermometer GTH 1170). It can be also powered by a DC/RF power supply via HN-Bias to generate a plasma that is necessary for substrate cleaning and surface etching.

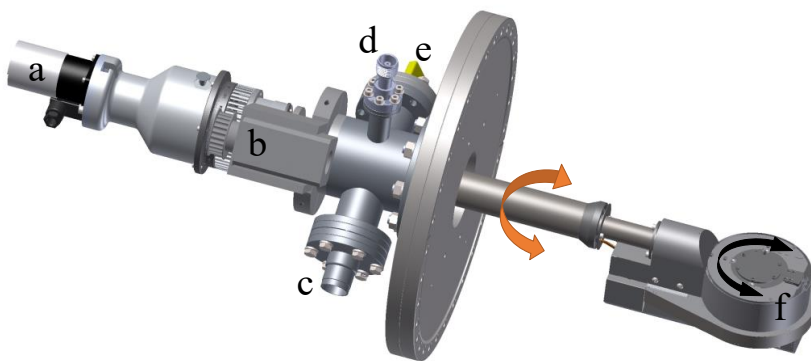


**Figure 11.** Schematic Image of the used sample holder consisting of two stepper motors (a,b) which give a specific rotation (black arrow) and tilting (brown arrow) of the sample, MS-style connector (c), HN-type feed-through (d), a type K thermocouple (e), and sample holder head (f).

There are two stepper motors (PD 42-3-1140). The first motor can supply a specific rotation of the sample. Whereas the second one is used to tilt the sample base to change the incidence angle of the sputtered material based on TMCL program commands. As mentioned earlier, there are three magnetrons, the incidence angle of the middle one is  $0^\circ$ . While each one of the left and right magnetrons makes a  $40^\circ$  angle of the perpendicular axis on the sample. The stepper motor supplies a resolution of 51200 micro-steps per single rotation. As well, it can read back the angular position (home position) which is necessary for the sample transfer process.

### 3.1.3 Load lock chamber and sample transferring

The load lock chamber facility saves much time of sample transfer in comparison with the evacuation of the sputtering chamber with a big volume itself. Accordingly, keeping the sputtering chamber pressure in the range of  $10^{-8}$  mbar (no vacuum break) during the placing of the substrate can be achieved. The pumping down of the load lock chamber by a turbomolecular pump (Pfeiffer HiPace 80) and the ACP-28 pump takes around 5 minutes for reaching a pressure range of  $10^{-6}$  mbar due to its small volume. This leads to the fast transfer of the substrate/sample to/from the sputtering chamber. Both pumps switch on/off simultaneously. They are controlled by the turbomolecular pump's controller. For the evacuation process, the ACP pump works only with the turbomolecular pump (Pfeiffer HiPace 80) to evacuate the load lock chamber to  $5.5 \cdot 10^{-5}$  mbar then works back with both turbomolecular pumps (HiPace 300, and HiPace 80). The switch of the ACP pump to work with HiPace 300 pump, HiPace 80 pump or both occurs via an electric magnetic valve. The chiller unit is also needed for heat removal from turbomolecular pumps.

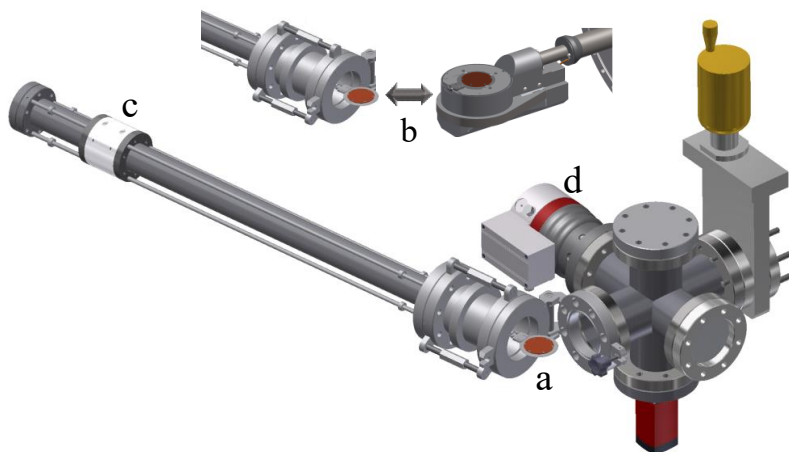


**Figure 12.** Schematic view of the hinge flange of the load lock chamber opening for sample mounting (a). The sample transferring from/to the sample holder (b) occurs by a magnetically coupled transfer rod (c) after evacuating the chamber via a turbomolecular pump (d).

The load lock chamber venting is realized by the turbomolecular pump's controller through nitrogen gas injection. Thereby, the ability to open the chamber and transfer the sample can be achieved. Additionally, the mounting of the sample in the load lock chamber is performed by opening the hinge flange as shown in Figure 12a. The sample is moved to the sputter chamber by a magnetically coupled linear transfer feedthrough (transfer rod). Such a process occurs through the opening of a UHV gate valve which separates between the load lock and sputtering chambers. The sample is transferred to the main chamber at a pressure  $1.10^{-5}$  mbar of the load lock chamber. For a perfect match and exact alignment of the transfer rod with the sample holder position, a flexible metal bellow is used to give correct tilting of the rod axis. The sample exchange process is carried out as illustrated in Figure 12b.

### 3.1.4 Nano-composites, particles, and films fabrication

Here, all the nanocomposites/nanoparticles were fabricated in a vacuum chamber. The chamber was initially pumped down to below  $10^{-6}$  mbar, while the pressure was  $3\text{--}5 \times 10^{-3}$  mbar during the sputtering. The sample holder of the device is guided to an angular rotation via a rotatable stepper motor to avoid the thickness gradient thus supplying a uniform film. The apparatus allows the preparation of a thin film nanocomposite composed of two dielectric and metal components with different filling factors. These thin films are deposited via co-sputtering of a dielectric target ( $\text{SiO}_2$ ,  $\text{TiO}_2$ ,  $\text{SiO}_{2-x}\text{TiO}_{2-1-x}$ ) sputtered via RF magnetron and a metal target (Au, Ag) sputtered via a DC magnetron. This technique allows the deposition on a wide range of substrates such as commercial black carbon tape, glass, Al foil and silicon substrates. The composite's filling factor was estimated based on the deposition rate. The rate of deposition of metal and dielectric were determined separately at the same gas flow rate and

pressure used for co-sputtering. In that case, the filling factor can be calculated by considering the equivalent film thickness of each component.

Moreover, the samples of Ag nanoparticles obtained at a thickness of 3, 4, and 5 nm coated commercial carbon tapes at room temperature (section 4.1) were fabricated based on the deposition rate (nm/min). Hence, the silver nanoparticles with low filling factor (Figure 13b) to high filling factor (Figure 13c) then film percolation (not shown here), and finally with continuous film formation (Ag-back-metal reflector, section 4.3) can be achieved by increasing the substrates exposure time.

The samples of Au-NPs obtained at a thickness of 5 nm used as a biosensor were prepared via sputtering at elevated temperatures (500 °C) on glass substrates. Whereas the silver nanoclusters obtained at a thickness of 8 nm were also produced by sputtering at high temperature on glass substrates and subsequently covered with different dielectrics composed of silica, aluminum nitride, and their mixture. The fabricated samples were kept inside the vacuum chamber until reaching room temperature when stage heating was used. It's worthy to mention that all metals were sputtered at a calibrated DC power of 20W, while the dielectrics were deposited at a calibrated RF power with forward power of 60Wf and reflected power of  $\geq 3$ Wr.

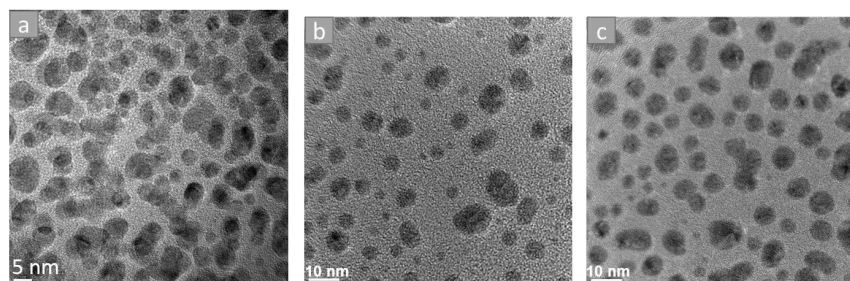


**Figure 13.** TEM characterization images of a 20nm Ag/SiO<sub>2</sub> nanocomposite film (a) and different silver thickness, 3 nm (b) and 5 nm (c) [Publication 1, Supporting information]. Reproduced with permission[64]. Copyright 2018, John Wiley and Sons.

The TEM characterization of the Ag/SiO<sub>2</sub> nanocomposite demonstrates that the embedded silver nanoparticles in a silica transparent matrix are in a diameter range of 4-5 nm (Figure 13a). On another hand, TEM images (Figure 13b,c) show the silver particles' morphology/distribution when the silver thicknesses are  $\approx$  3 and 5 nm. As well, the hybrid dielectric film of silica-titania composite was characterized by TEM as shown in Figure 14a. The TEM image shows that the film is amorphous, owing to the immiscibility of the dielectrics, i.e., SiO<sub>2</sub> and TiO<sub>2</sub>[69]–[72]. A TEM image in Figure 14b clarifies the random distribution of the gold nanoparticles that are close to each other embedded in the hybrid (TiO<sub>2</sub>/SiO<sub>2</sub>) matrix.

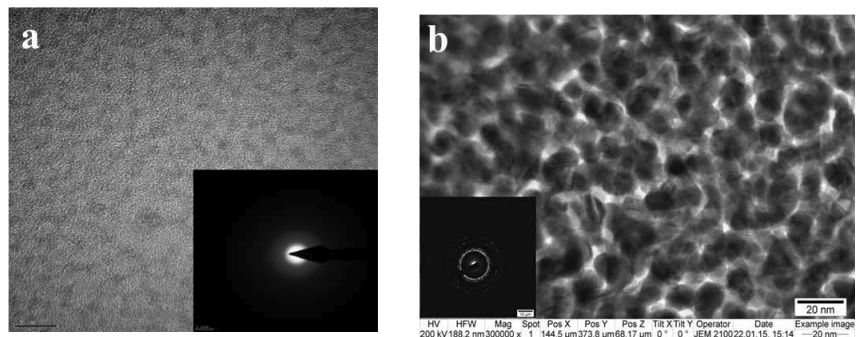


**Figure 14.** a) TEM image of the TiO<sub>2</sub>-SiO<sub>2</sub> hybrid film. The inset image shows the diffraction pattern of the hybrid film. b) TEM image of the 40% Au/ (TiO<sub>2</sub>/SiO<sub>2</sub>) nanocomposite with an amount ratio of 50/50 of the dielectrics. The structure diffraction pattern is shown by the inset image [Publication 3]. Reproduced with permission[13]. Copyright 2019, John Wiley and Sons.

Finally, the production of the fabricated materials including nanocomposites/nanoclusters and films via magnetron sputtering is reproducible, repeatable, and scalable owing to the precise control of the deposition parameters. For instance, in order to achieve reproducible and repeatable samples at an expanded production scale, some parameters should be taken into consideration. First, the deposition rate should be newly calibrated once installing the target material/magnetron source. Second, all the deposition parameters such as sputtering gas pressure, DC power, RF power including the forward/reflected power values, the distance between the target and the substrate, and the angle of incidence of the sputtered atoms should be constant. Regarding the production of Ag and Au nanoclusters samples fabricated at elevated temperature, the heating procedure according to the power-temperature curve (Heater Stage Calibration Data) of the sample holder's manual should be achieved for the selected temperature. One of the key characteristics in taking this research to the market is the relative stability/shelf-time while maintaining the same performance/visual aspect. In this context, emphasizing the stability limit of most evaluated samples (including the spin-coated samples) within the scope of this thesis were shown considerable stability limits with no physical/chemical deterioration with an optical readout over the timeframe defined for the thesis work (i.e., Months that would extend to up to a year(s) depending on the sample material).

In terms of scalability, the used technique enables a variety of substrates can be coated with a broad range of materials in different shapes and forms that are scalable to sizeable areas. However, scaling the magnetron sputtering is not a straightforward process due to the fact that changing chamber/target dimensionality results in a significant change in the mean free path along with affecting the plasma stability/propagation within the target field [73].

### 3.2 Leidenfrost technique

The Leidenfrost technique is used as a basis of a green nanofabrication method[74]–[76]. Through that method, the self-organized metaparticles could be fabricated within a levitated droplet placed on a preheated plate. The chemical synthesis process occurs in the droplet's overheated area followed by the eruption of the synthesized metaparticles to the colder region[75]. Here, the synthesis process of CuO rice-shaped structures starts once the main material of 50 mL containing an aqueous copper salt solution (10 mM with pH = 8) is dropped through a glass burette with a feed rate of  $1 \text{ mL } 25 \text{ s}^{-1}$  on a preheated aluminum plate ( $300^\circ\text{C}$ ). Consequently, the solution color through 45 sec turns promptly black as a sign of forming CuO particles as shown in Figure 15a. Subsequently, the yield can be simply collected as a powder. It is worthy to note that the particle's morphology and size can be controlled by manipulating the pH value. In this dissertation, we were opted to examine the commonly utilized step-wise scaling procedure at which the scaling process occurs at different expansion schemes. In this regard, we were successful at expanding the producibility of Leidenfrost reactor from batch droplet sized reactor up to puddle with a continuous precursor solution feedback in semi-flow pattern while maintaining the same chemical output. Indeed, with such methodology the production of up to gram(s)-scale well defined nanoparticles is feasible. In brief, the scaling process of Leidenfrost nanofabrication can be achieved via applying an aqueous solution through a liquid dispensing system placed over a hot plate with a pre-defined dispensing rate, thus producing CuO nanopowder within a scalable manner in comparison with common Leidenfrost droplet (Figure 15a).

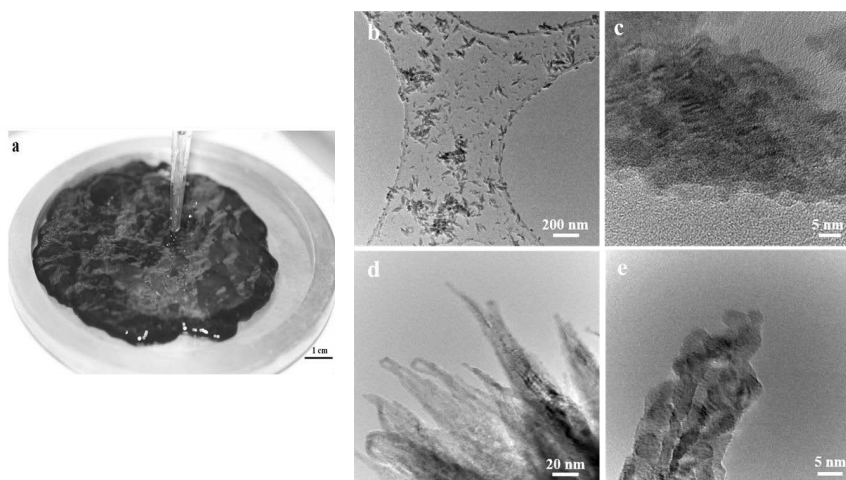


**Figure 15.** The Leidenfrost droplet “green nanochemistry”. a) Camera image of the levitated Leidenfrost droplet forming CuO particles including upscaling process of nano synthesis to a 50 ml aqueous copper salt solution. b,d) The TEM bright field images of two different morphologies for CuO structures (rice- and star-like morphology). c,e) The high resolution TEM micrographs of the same CuO structures [Publication 2]. Reproduced with permission[65]. Copyright 2019, John Wiley and Sons.

The structures that were produced at the same concentration but with a different pH value (from 8 to 10.5) are shown by the TEM images in Figure 15b,c,d,e. TEM characterization showed the self-organization and morphology of the nanostructures. In this regard, TEM bright-field Images prove the CuO structures' condensed arrangement irrespective of their morphology as shown in Figure 15b,d. As an outstanding feature, the high-resolution TEM micrographs in Figure 15c,e demonstrated that the structures are based on self-organized nano-constituents.

### 3.3 Spin-coating technique

A uniform thin film onto flat substrates can be reached by a spin-coater machine. The thickness of the film can be varied by change of the concentration and/or the velocity as well. A spin coater (Laurell, WS-650-23NPP) as shown in Figure 14, was used. A mixture of CuO (different size and morphology) aqueous dispersed in PVA aqueous solution (used as the matrix of the composite) were spin-coated on a glass substrate in two steps of speeds. These spinning speeds were 400 rpm for 4 sec and then 7000rpm for 60 sec. The mixture solution was deposited on the glass surface while holding in the vacuum chuck of the spin coater. Then the sample starts spinning till the film gets dried. Therefore, the CuO/PVA composite film is ready for the characterization process. The fabricated films can be accomplished easily in a reproducible manner. The spin coating device allows accurate control over the process parameters; thus, reproducibility can be achieved by considering some parameters such as the speed, steps, time, and concentration of the coating solution. Finally, such a technique can be applied to coat small areas of substrates (a few centimeters squared) as presented here. It also enables scalability where some parameters such as the motor torque, the size of the hosting chamber, and the volume of the solution should be taken into account[77], [78].

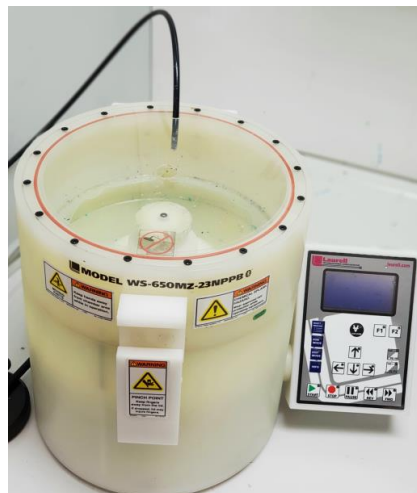


**Figure 16.** Camera image of the Spin-Coater device, Laurell Model WS-650-23.





## 4. Results and discussion

In this chapter, we present the polarizonic reflective coloration and BW effect of disordered metallic/oxide metaparticles and their potential in a diverse range of advanced applications such as energy-saving, e.g., perfect “colored” solar absorbers (Publication 1, 2, and 3) and biosensing (Publication 1).

### 4.1 Tailored perfect colored absorber (Publication 1)

As above discussed (section 1.6), when the light irradiates dipoles, they oscillate strongly at the resonance frequency, so radiating secondary waves[59], [79], [80]. Therefore, the polarizonic specular reflection peak arises from radiated field created by the superposition of these secondary waves. In this regard, silver nanocomposite (i.e., Ag nanodipoles hosted by a silica matrix) thin film with a 20% filling factor was fabricated via magnetron co-sputtering. The total reflection of the Ag nanocomposite deposited on a glass substrate was measured under oblique incidence. As shown in Figure 17a, the polarizonic reflection peak appears at 442 nm (blue range) (s and p-polarized reflection spectra shown in Publication 1). By using a blackbody (carbon tape) as a substrate thus the light transmission and diffuse scattering are blocked[64], the blue color can be visualized as illustrated by the camera image in Figure 17b. As mentioned earlier (section 1.6) that both polarizonic reflection and absorption take place at the same resonance wavelength. Thus, the polarizonic reflection resonance (PRR) peak can be tuned through the common plasmonic parameters, such as nanoparticle’s size, filling factor, medium refractive index, and the type of dipole. In this respect, Ag nanoparticles obtained at a thickness of 3, 4, and 5 nm sputtered on black substrate such as carbon tape and a transparent polymer foil. As shown by the photograph in Figure 17c, the polarizonic reflection colors (PRCs) (dark blue, dark green, and yellowish-green) of Ag NPs ( $\approx$  3, 4, and 5nm) appeared on the black carbon tape substrates. Additionally, the specular reflectivity of these samples was measured, as illustrated in Figure 18a. On the other hand, the plasmonic colors appeared on the transparent polymer foils as shown by the photograph in Figure 17c. The transmission of the samples is recorded, as illustrated in Figure 18b. The results show that a strong tuning of the reflective and extinction coloration can be achieved by changing the Ag thickness (i.e., the resonance redshifts with increasing the thickness).

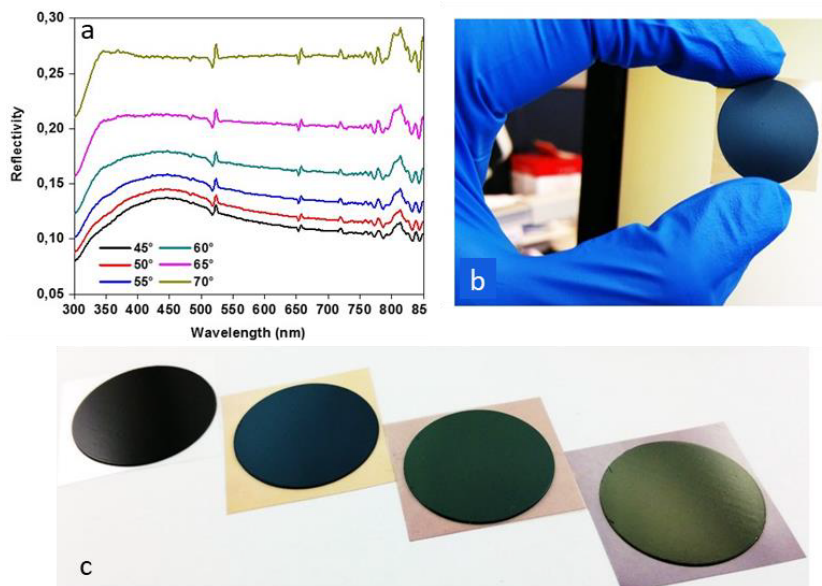


**Figure 17.** PRC visualization of metallic NPs/nanocomposite based on blackbody substrate. a) The specular reflectivity measurement of a 20 nm thick silver nanocomposite (Ag/SiO<sub>2</sub>) in different angles of incidence. b) Photograph of a carbon tape covered with the abovementioned Ag nanocomposite. c) Camera image of samples including the silver films deposited with different thicknesses  $\approx$  3, 4, and 5 nm (from left to right) on transparent polymer foils and black carbon tapes (the first substrate act as a reference sample, has no Ag coating) [Publication 1]. Reproduced with permission[64]. Copyright 2018, John Wiley and Sons.

Also, it was experimentally noticed that PRC has higher environmental sensitivity compared with that of plasmonic absorbed/transmitted color. This is due to its dependency on the propagation delay (i.e., the RI's real part changes). To visualize this matter, Ag nanoparticles sputtered at an elevated temperature (500 °C). Subsequently, the Ag NPs samples were coated with different dielectric matrices composed of silicon dioxide (SiO<sub>2</sub>), aluminum nitride (AlN), and their mixture that prepared at various composition ratios and different thicknesses. Owing to intensity dependency, the visual distinction of the colors of the coated samples was challenging in transmission mode, as illustrated in Figure 18c. In contrast, the samples based on a black background (reflection mode) show distinct rainbow colors, each color represents a particular coating material as seen in Figure 18d. In other words, such a difference in reflection and transmission has great potential for environmental sensitivity, as we will discuss below (section 4.4).

In conclusion, the creation of vivid structural reflective coloration using disordered metallic nanoclusters on a surface or covered/embedded by/in a dielectric medium was presented. As a practical application, this polarizonic structural coloration will play a substantial role in the design of perfect solar materials with vivid colors in simple and cost-efficient way.

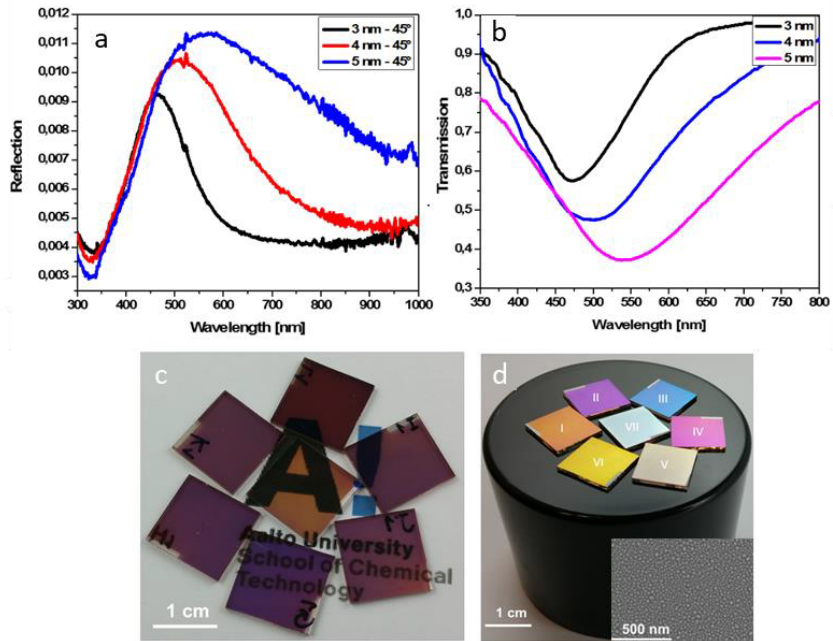


**Figure 18.** a) Polarizonic reflection measurement of the same coated samples illustrated in (Figure 17c). b) Transmission measurement of the same samples illustrated in (a) but deposited on transparent polymer foils. c) The photograph of the samples including Ag NPs on glass substrates then coated with various dielectrics of Aluminium nitride, Silica, and the composites showing very feeble color contrasts in the transmission state. d) Camera image of the same samples shown in (c) but placed on a black substrate. The samples marked as I through VII include different dielectric thin coatings of AlN, silica, and the mixtures (composites) thereof with various thicknesses and compositions (I: 60 nm thick 70% AlN-SiO<sub>2</sub>, II: 80 nm thick 50% AlN-SiO<sub>2</sub>, III: 80 nm thick 70% AlN-SiO<sub>2</sub>, IV: 80 nm thick AlN, V: 80 nm thick SiO<sub>2</sub>, VI: 60 nm thick 50% AlN-SiO<sub>2</sub>, and VII: without coating layer). Inset SEM image illustrates the distribution of the Ag NPs (8 nm thick) deposited at 500 °C utilized in the samples shown in (c,d) [Publication 1]. Reproduced with permission[64]. Copyright 2018, John Wiley and Sons.

In the next section, we show the combining of such plasmonic structures “nano-composites” offering polarizonic reflection resonance with a conductor possessing broad reflection, resulting in polarizonic interference. Such interference located at the resonance position has been exploited for the design of flexible solar aluminum foils with attractive colors.

## 4.2 Colored solar aluminum kitchen foils (Publication 3)

Aluminum (Al) with distinctive colors could be realized by an anodizing process[81], [82] with or without dyeing, i.e., the inclusion of artificial nanoparticle pigments. Through the anodizing process, the aluminum surface can be a good absorber rather than a reflector. Despite the simplicity of this process, its application for the fabrication of the solar Al foil is difficult, as the foil is mechanically fragile. Furthermore, the use of hazardous chemicals in this process is considered the most problematic issue. Also, the environmental concerns where the harmful byproducts resulting from the chemical compounds' dissociation act a great challenge[13]. To reduce/overcome such problems, we produced here a colored Al foil with shiny and matt coloration, based on a very thin coating enabling tuning the reflectivity and absorptivity, as a great alternative fabrication method.

The design of a selective solar Al foil can be achieved usually by interference-based multilayer thick coatings considering the quarter lambda rule. In that case, the optical response of such structure alters by changing the incidence angle through the day, where the transmission of the light through the structure's layers is angular or it can be even polarization-sensitive[13], [83]. In this work, we introduce a new generation of inexpensive and effective energy kitchen Al foils in vivid artificial structural coloration including a gold color based on polarizonic interference. Such polarizonic interference i.e., interference of the specular reflection of metallic nanostructures occurring at the optical frequencies with a broad reflection of a conductor, was utilized as an innovative design tool for the creation of these structural colors. Here, the fabrication of such colored solar Al foils (with absorptivity of more than 90%) was realized by depositing disordered nanostructures on an Al kitchen foil enabling distinctive metallic, shiny, and matt appearance. Additionally, these fabricated structural colored samples are omnidirectional and regardless of the angle of the incidence/polarization.

The classical free electron theory can explain some metal's reflectivity as a continuous field. Thereby, different metals such as aluminum and silver show a broadband reflection in the visible and IR range and this clarifies their gray appearance. In other words, the gray color gives rise to the absence of the localized reflection "discontinuous" of plasma oscillation at the visible frequency. Nevertheless, gold appears in a golden color, this is due to the existence of a localized reflection "discontinuous" at the plasma frequency (as described by the Lorentz classical harmonic oscillators) and a "continuous" broad reflection of the free electron states. This gives rise to a reflection drop in the blue range of visible frequencies (440-490 nm). Based on that, it can be realized that the polarizonic interference can appear when a "continuous" broadband reflection of a grey metal or even a semi-metal interferes with a "discontinuous" localized state of polarizonic reflection of plasmonic NPs, as shown in Figure 19a.[13]

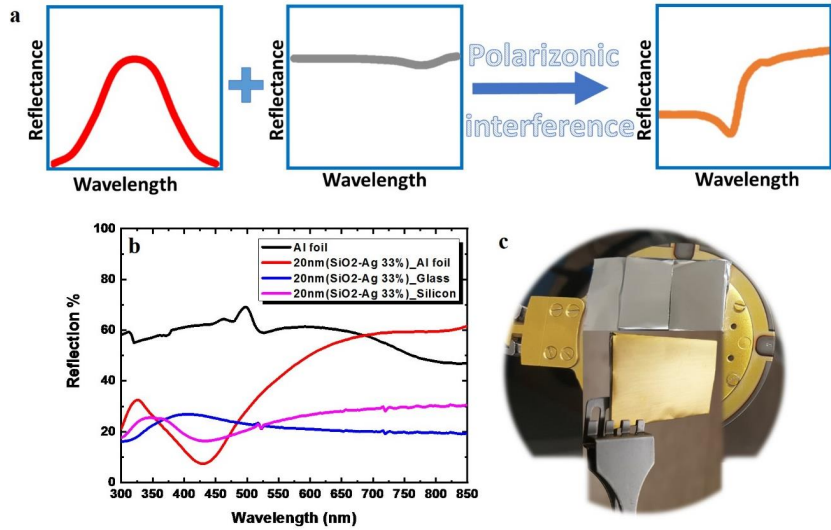


**Figure 19.** The polarizonic interference concept. a) Schematic demonstration of the interference between specular localized reflection and broad reflection of a conductor, i.e., polarizonic destructive interference. A reflection drop at the resonance frequencies occurs due to this destructive interference. b) The polarizonic reflectivity of a 33% Ag/SiO<sub>2</sub> nanocomposite on glass exists at the blue range. Such interference and thereby the reflection drop can be clarified via coating of gray substrates such as an aluminum foil and/or Silicon layer by the silver nanocomposite. c) The Al foils and stainless-steel substrates covered with the nanocomposite show a golden color via the polarizonic interference phenomenon [Publication 3]. Reproduced with permission[13]. Copyright 2019, John Wiley and Sons.

To confirm this point, grey appearing substrates such as aluminum foil, silicon, and stainless steel were coated with a 20nm thin layer of silver-silica nanocomposite with 33% Ag filling factor, herewith giving rise to the presence of polarizonic interference. Such interference occurs close to the PRR peak that occurs at the blue range of visible frequencies, Figure 19b. As a result, the induced optical response of the coated substrates is equal to gold (i.e., golden appearance) as shown in Figure 19c. Additionally, by varying the filling factor of the composite, the golden color can be controlled. For example, the foil with a titan silver color can be achieved by using a composite comprising 20% Ag NPs, as shown in Figure 20a. The polarizonic reflection measurements, i.e., total, s, and p-polarized reflections of 20% Ag-SiO<sub>2</sub> nanocomposites covered Al foil sample under oblique incident were presented, as illustrated in Figure 20b-d. The results emphasize the angle and polarization independence of the polarizonic interference-effect. As noticed, when the incidence angle changes from 45° to 75°, the minima at 400 nm stays almost constant in all reflections.

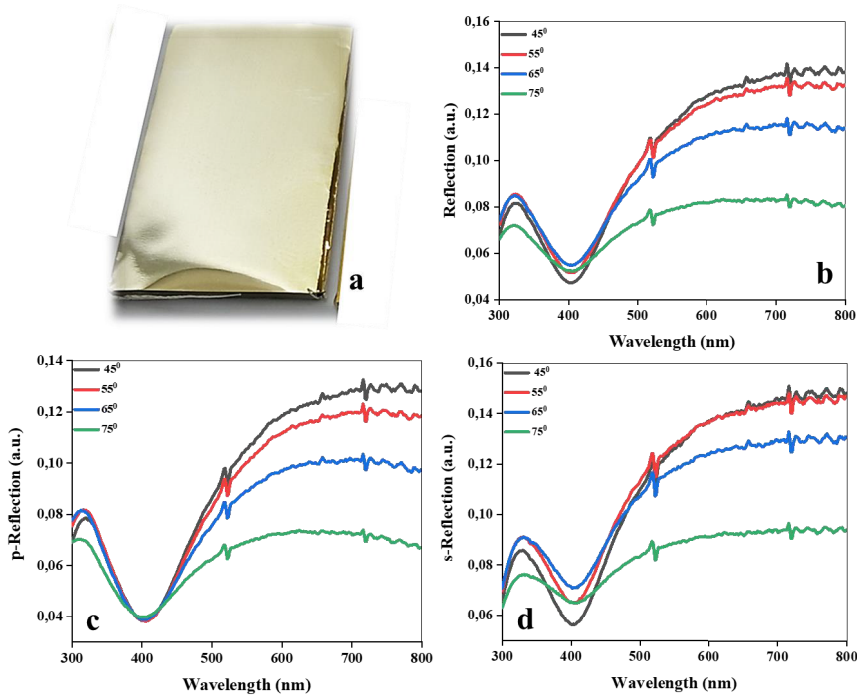


**Figure 20.** The angle independency “omnidirectional” of the PRC based on interference-effect. a) Al foil coated with a 20% Ag/SiO<sub>2</sub> nanocomposite is a titan color for the foil by the polarizonic interference-effect. b-d) The total, p-polarized, and s-polarized reflectivity spectra of a 20 nm Ag/SiO<sub>2</sub> nanocomposite on an Al foil at various angles of incidence [Publication 3]. Reproduced with permission[13]. Copyright 2019, John Wiley and Sons.

As obviously shown in Figure 20b, the dipolar destructive interference plays a fundamental role in the polarizonic interaction. Moreover, the finite difference time domain (FDTD) method support that argument, where a 20 nm Ag/SiO<sub>2</sub> nanocomposite was simulated based on such a method. The simulation results showed the remarkable properties of the cooperative action of the Ag NPs (5 nm) as well as their interference with a grey conductor. The embedding of such NPs in a dielectric medium causes electromagnetic confinement and spatial radiated field in the Z direction. Such radiation differs significantly from dipolar coupling that existed in the X-direction, as illustrated in Figure 21a(left). On other hand, as seen in Figure 21a(right), the electromagnetic fields are debilitated when the Ag/SiO<sub>2</sub> composite deposits on a semi-conductor (Si). As a result, the dipolar interference between the excited dipoles and their images induced in the conductor surface creates a non-radiative quadrupole mode leading to an antireflection event and rules the design of omnidirectional polarizonic interference[13].

As aforementioned, the PRR of metallic nanocomposites can be tuned by varying the shape, size, and dielectric constant of the surrounding medium of their metallic objects. Here, the resonance is adjusted by combining two dielectric matrices (hybrid dielectric matrix), where the RI can be changed by varying the ratio of that hybrid matrix's components (The refractive indices (RIs) of the hy-

brid films were determined by a model-based ellipsometry data analysis, Publication 3). Since any slight manipulating of the matrix's composition gives rise to a strong tunability in the reflection band, thus the range of the operating frequency wherein the polarizonic interference takes place can be tuned.

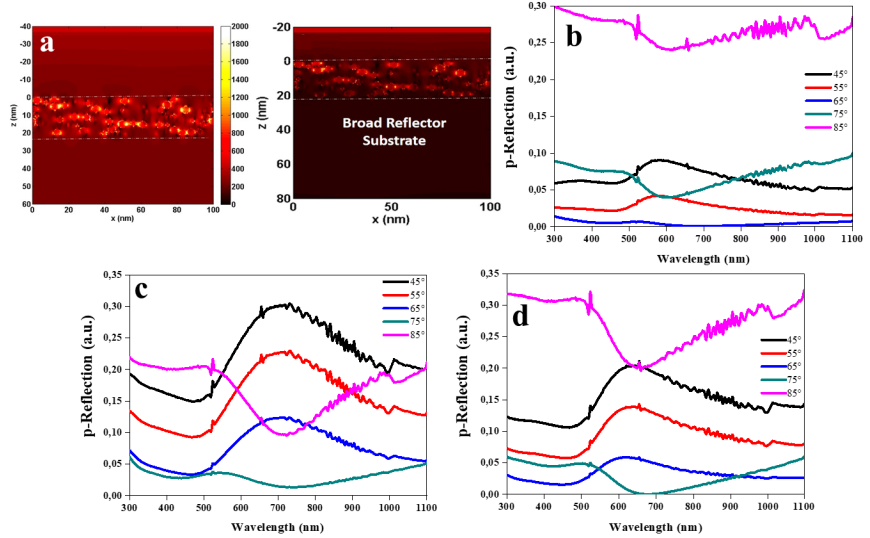


**Figure 21.** e) The FDTD simulation of the cross-section of a silver-silica nanocomposite with a 20% filling factor (Ag NPs are arbitrarily arranged separately) irradiated with light (430 nm) showing the electrical field amplitude distribution as alone (left) and as covered a grey semi-metal (Si) substrate (right). b,c, and d) the p-reflectivity of 40% Au/SiO<sub>2</sub>, 40% Au/TiO<sub>2</sub>, and 40% Au/(50/50) SiO<sub>2</sub>-TiO<sub>2</sub> nanocomposites, respectively, where the PRR is tuned by the change of a hybrid matrix's composition [Publication 3]. Reproduced with permission[13]. Copyright 2019, John Wiley and Sons.

The polarizonic reflection spectra of the Au/SiO<sub>2</sub>/TiO<sub>2</sub> nanocomposites coated glass substrates were measured at a constant gold ratio (40%) and different ratios of TiO<sub>2</sub>/SiO<sub>2</sub>, as shown in Figure 21b-d. The results show a significant resonance redshift with the rising of the TiO<sub>2</sub> ratio in the matrix as well as the intensity of the reflectivity increases. Indeed, the abovementioned polarizonic interference phenomenon can be used as a base for a new generation of double-layered perfect solar absorbers with vivid colors. Additionally, such polarizonic interference can be readily adjusted by the type and the filling factor for both the dielectric matrix and metallic nanostructures, respectively. In this regard, as a practical application for this interference concept, flexible colored solar foils were fabricated through a kitchen Al foil coated with a thin film of gold nanocomposite with different volume fractions and various dielectric hosts.



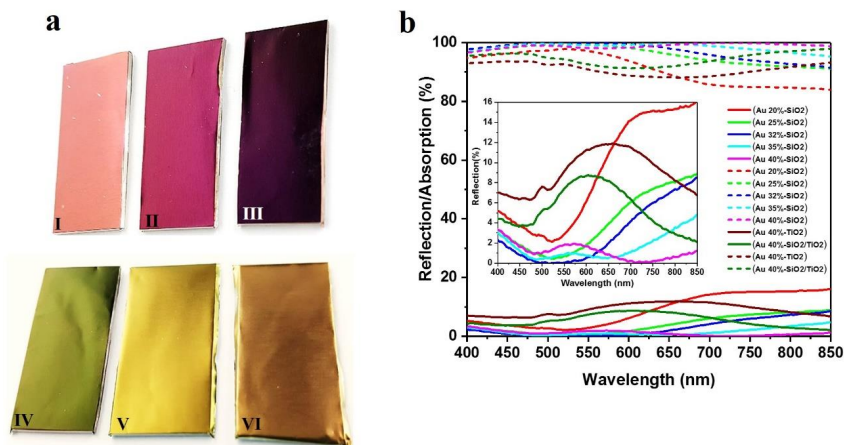


**Figure 22.** Colored perfect absorption samples composed of the polarizonic Au nanocomposites coated flexible Al kitchen foil. a) The tailored perfect-colored absorbers presented by the (Au/SiO<sub>2</sub>)/ Al foil by varying the filling factor in distinct colors: I; 20% Au/SiO<sub>2</sub> (rose red), II; 25% Au/SiO<sub>2</sub> (wine red), III; 32% Au/SiO<sub>2</sub> (purple), and IV; 40% Au/SiO<sub>2</sub> (green), respectively. While in the case of replacing the silica Matrix with titania as in V; 40% Au/TiO<sub>2</sub> and a hybrid matrix as in VI; 40% Au/ (50/50) (TiO<sub>2</sub>/SiO<sub>2</sub>), the colors change to golden and brown, respectively. b) The reflection/absorption spectra of the samples when the Au filling factor and the dielectric host change. The inset Figure shows that the appeared colors are due to the polarizonic reflection and interference effect of the absorber concerning its change composition [Publication 3]. Reproduced with permission[13]. Copyright 2019, John Wiley and Sons.

The fabrication process of the solar kitchen Al foil samples was done via the co-sputtering of the Au and dielectric (SiO<sub>2</sub>, TiO<sub>2</sub>, and SiO<sub>2</sub>/TiO<sub>2</sub>) materials on a  $\approx 0.02$  mm thick kitchen Al foil. By the change of the Au filling factor and the host dielectric medium, such foils appear in shiny and matt coloration such as rose red, wine red, purple, green, golden, and brown, as shown in Figure 22a (I-VI), respectively. The absorption/reflection spectra of these coated samples are shown in Figure 22b.

In conclusion, the design of flexible solar Al foils in vivid reflective colors including goldish ones was presented based on the polarizonic interference concept. We believe that such a concept will play a significant role in establishing a new class of colored solar absorbers. It is worthy to note that the presented flexible solar materials were fabricated based on Al kitchen foil which is flexible thus easily shapeable, and inexpensive as well. Finally, since the fabrication technology used here is a sputtering technique that is industrially established, the proposed method introduces interesting possibilities for designing perfect colored absorbers.

All the applications that have been highlighted in sections 4.1 to 4.2 were achieved based on the polarizonic reflection phenomenon of metallic nanodipoles with a size range of few nanometers. In the next section, we designed and fabricated a perfect solar absorber material using the polarizonic response of the transfective oxide metaparticles synthesized via Leidenfrost green chemical reactor as an efficient alternative for noble metal nanomaterials.

### 4.3 Perfect black solar absorber (Publication 2)

Oxides have been utilized in multiple advanced applications in terms of energy harvesting, such as thermal photovoltaics and perfect solar absorber[65], [84], [85]. Specifically, the greenly synthesized oxides which are used in the manufacture of surfaces able to control solar radiation have attracted attention. Thus, ultrathin coatings based on such oxides are strongly desired for the design of solar absorbers and/or solar transfective materials. In other words, the design of the nanocoatings that can show transparency and reflectivity at the same time over the visible spectrum is highly demanded. Such coatings are considered unique coatings because they assure lower power consumption (i.e. absorptivity is negligible in the visible range) for various applications[65]. In this regard, the self-organized oxide metaparticles (CuO) with varied sizes and morphology have been produced here via Leidenfrost nanochemistry. The synthesized metaparticles that are in mesoscopic regime, are composed of nanoconstituents, they are closely spaced and whose sizes smaller than the light wavelength. As a result, the light can be perfectly manipulated in confined inter gaps. Thus, when the light illuminates the fabricated structures, the polarizonic reflection takes place whereas the structures stay transparent, i.e., the medium becomes transfective “lossless.” Such transfective ability is due to their electronic polarization response at visible frequencies.

As abovementioned (section 3.2), the Leidenfrost reactor is solely constructed with a hot plate supplying the required temperature. The synthesis process starts once the main material containing an aqueous copper salt solution is placed in a droplet form on a preheated aluminum plate, as shown in Figure 15a. In the case of increasing the solution's pH value from 8 to 10.5, the concentration of both hydroxide ions and negative charges inside the Leidenfrost droplet increase. Thereby, the yield of particles becomes higher, and the particle size increases with different morphology. Based on that, the CuO metaparticles were produced in different sizes and morphology, i.e., rice ( $\approx 50\text{nm}$ ) and star ( $\approx 600\text{nm}$ ) like morphology. These structures were produced at the same concentration but at a different pH value, as shown by the SEM images in Figure 23a,b (XRD spectra shown in Publication 2).

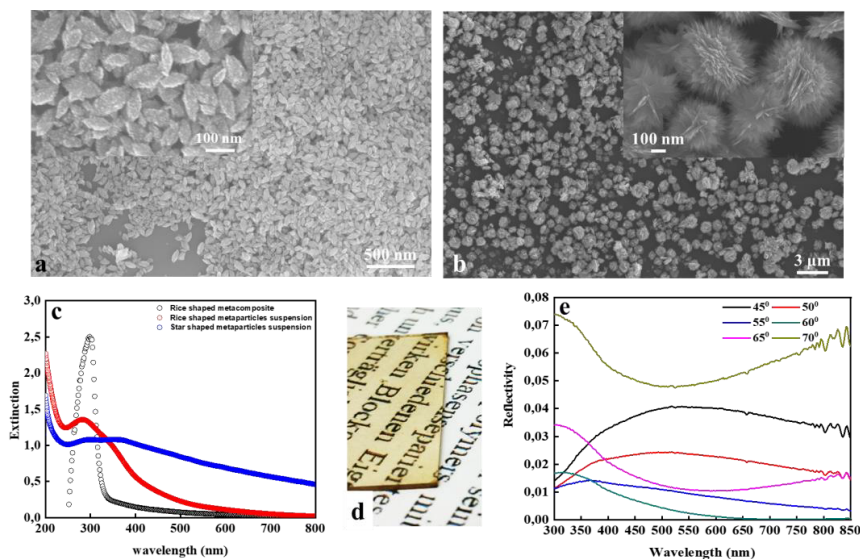


**Figure 23.** The transfective composite is based on the oxides metaparticles of levitated Leidenfrost droplet. a) SEM image shows the rice-shaped CuO metaparticles at two various magnifications synthesized by leidenfrost reactor at pH of 8. b) SEM image illustrates the star-like morphology of CuO particles fabricated at the same precursor concentration as rice-shaped structures in a) but at pH of 10. c) Extinction spectra of the solid metacomposite comprising the rice-shaped structures against that of the aqueous suspensions samples comprising the rice and star-shaped particles. d) Photograph shows the transparency of the rice-shaped CuO-PVA metacomposite film. e) p-polarized reflection measurement of the 50 nm thick rice-shaped CuO-PVA composite in various angles of incidence [Publication 2]. Reproduced with permission[65]. Copyright 2019, John Wiley and Sons.

When such oxide metaparticles “dipoles” interact with the light including the p-polarized component, the collective oscillation of bound and free electrons occurs thus the displacement of the electron cloud takes place. Eventually, this leads to resonating specular reflection. Indeed, the optical properties of the metal oxide particle can be described based on their electronic transition (i.e. their bandgap).[65] Here, we report the specular reflection of these metaparticles at the visible wavelength that is achieved due to their electronic polarization “polarizonic response.” Accordingly, A transfective “nonabsorbing/transparent” coating based on the oxide’s polarizonic response at the visible wavelengths was accomplished.

By using the spin coating fabrication technique (section 3.3), the transfective layer was made of 50 nm thick metacomposite composed of CuO rice-shaped metaparticles incorporated in polyvinyl alcohol (PVA) polymer host medium. Such composite appears with high transparency, as confirmed by extinction measurements (Figure 23c). Despite there is no marked resonance peak in the extinction spectrum of the sample, it shows a yellow color (camera image, Figure 23d) which implies its non-absorbing nature. Thereby, the appearance of yellow color can be attributed to the film’s polarizonic reflectivity. As shown in Figure 23e, the p- polarized reflectivity spectrum of the CuO/PVA metacomposite shows a broad resonance peak at 550 nm. Thus, the origin of the emerged yellowish color is readily recognized. On another hand, the CuO star-shaped structures nanocomposite could not show an optical response, as induced by a

rice-shaped one. Based on that, the metacomposite film comprising the rice-shaped metaparticle can be used as a transfective coating at the visible spectra.

As a practical application, a perfect solar absorber can be achieved based on selective polarizonic interference. Such interference occurs between the transfective coating (rice-shaped CuO/PVA metacomposite) enabling selective specular reflection and the underlying silver mirror presenting a broad reflection at the visible frequencies. Whereas this interference does not exist in the presence of a non-resonating composite such as a star-shaped CuO/PVA composite. In Figure 24a, the configuration of the mechanism is illustrated where a 50 nm thick CuO rice-shaped metacomposite is covered with a 60 nm thick Ag layer. The reflection and absorption spectra as well as the sample of black solar absorber shown by the camera image are illustrated in Figure 24b,c (left), respectively. Whereas the sample based on CuO star-shaped nanocomposite could not show the ability of solar absorbing i.e., black color, as shown by the photograph in Figure 24c (right).

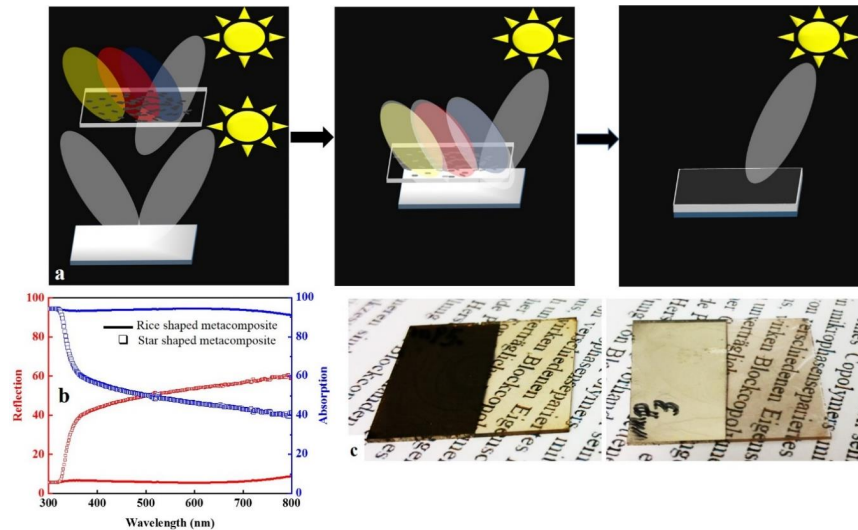


**Figure 24.** The thinnest perfect solar absorber via transfective metacomposite coating based on interference-effect. a) Schematic shows in three steps the construction of the perfect solar absorber composing of the transfective (rice-shaped CuO/PVA) metacomposite coating and an underlying silver mirror layer. b) Reflection-absorption spectra show the fabrication of a perfect black absorber by the metacomposite thin-coating. c) Photographs show the optical properties difference of the rice-shaped CuO/PVA metacomposite (left) and star-shaped CuO/PVA (right), this illustrates the potential of the rice-shaped structures for exploitation as a perfect absorber [Publication 2]. Reproduced with permission[65]. Copyright 2019, John Wiley and Sons.

Taking together, a novel coating material that can show polarizonic reflection and at the same time is transparent, was achieved. Such coating works based on lossless oxide metaparticles containing self-organized nanoconstituents which are produced via “Leidenfrost” green chemical reactor. It is relevant to note that such a remarkable feature (i.e., transfective) of that coating is morphology-dependent. Using the rice-shaped metacomposite with a back-metal reflector allows the design of the thinnest oxide perfect solar absorber ever where the absorptivity intensity is near to 100% at the visible spectrum.

In the abovementioned sections, we concentrated on showing the potential of the polarizonic effect of metallic/oxides nanostructures in an energy-saving field. On the other hand, concerning biomedicine e.g., biosensing field, plasmonic has been successfully used to sense a wide range of biological molecules. In this regard and based on our results as shown earlier, the ability of the plasmonic structural system to achieve high environmental sensitivity by PRR position made us curious to implement it in the biosensing area. In the next section, the visualized bulk biodetection based on specular reflective coloration and plasmonic Brewster Wavelength (BW) effect will be presented in detail.

#### 4.4 Naked-eye bulk biodetection (Publication 1)

At the localized surface plasmon resonance (LSPR), we could see the occurring of the polarizonic reflection as mentioned earlier, as well as the Brewster Wavelength (BW) phenomenon that is considered an interesting new feature. Here, the polarizonic reflection and BW phenomenon of metallic NPs at the resonance frequency have been utilized as a new base for the naked-eye and bio-detection of analytes including the bulk state, i.e., bulk RI monitoring. Indeed, such bulk detection is considered a huge challenge for traditional plasmonic biosensor based-absorption[86]. Since any changes in molecular polarizability of the surrounding medium in the bulk state are not detected or visualized by the localized plasmon[64].

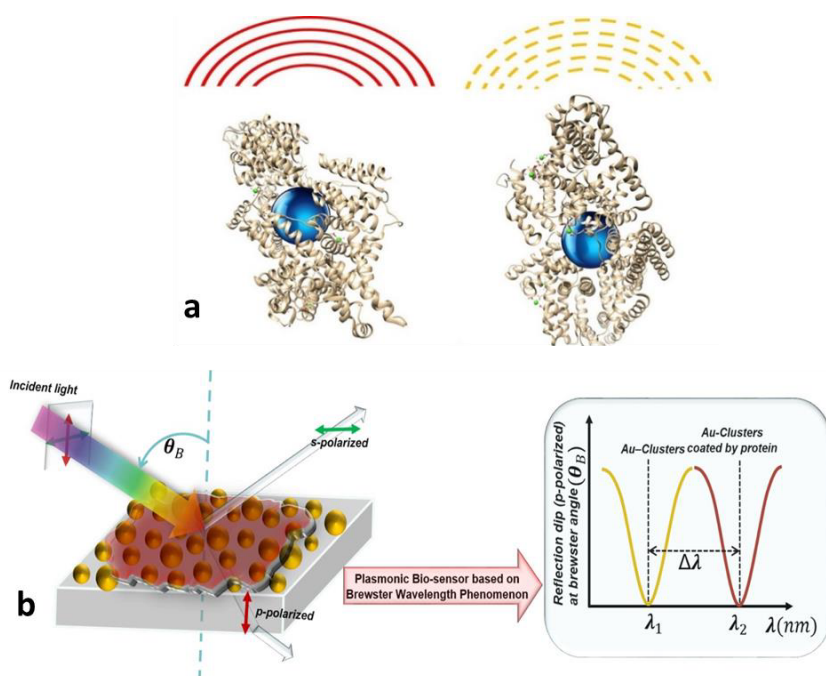


**Figure 25.** a) Schematic illustration of the optical appearance of plasmonic dipoles coated with bovine serum albumin (BSA) protein comprising bulk material when conformational of BSA changes. Thereby, the speed of the wave's propagation alters, resulting in appearing of different radiation colors. Whereas, the plasmonic blue color of the nanodipoles does no change remarkably. b) Schematic demonstration of the phenomenon's mechanism for bulk biodetection where p-polarized light hits the sample (analyte on NPs platform) and its wavelength shifts [Publication 1]. Reproduced with permission[64]. Copyright 2018, John Wiley and Sons.

The polarizonic reflection wave in the surrounding arises from the cooperative dipolar coupling, where the NPs “nanodipoles” act as microscopic antennas that can receive and store the energy whereas radiating the light to the far-field. Thereby, the information of detection can be transferred to the observer via a specific radiated/reflected color relying on the propagation delay by the surrounding matrix, i.e., the RI's real part. As well-known, the wave speed equals

the product of wavelength and frequency. Thus, the changing of the wave speed by the molecular polarizability of the matrix can be simply defined by a corresponding variation in the radiated wavelength if the oscillation frequency stays constant. As a result, the different reflective colors appear while the plasmonic color is still constant against the change of matrix, as schematically shown in Figure 25a.[64]

The plasmonic BW in which the reflection of p- polarized light is negligible at a certain angle shifts from tens of nanometer (nm) to a few hundreds of nm. Such a technique allows bulk bio-detection as well as examining several analytes at a constant angle. The sensitivity (S) for the biosensor can be estimated by equation (11):

$$S_R = \frac{1}{R(\lambda)} \frac{\partial R(\lambda)}{\partial n} \bigg|_{\lambda=\lambda_0} \quad (11)$$

where  $R$  is the reflection,  $\lambda_0$  is the minimum reflection wavelength in air, and  $n$  is the refractive index. When the reflection in (Eq. 11) is closest to zero, the sensitivity,  $S$ , reaches its maximum.[64], [87], [88]

Our biosensor “platform” was fabricated via magnetron sputtering by depositing gold NPs at 500 °C on a glass substrate (optical & SEM characterization illustrated in Supporting Information, Publication 1). The gold NPs were preferred over the other plasmonic materials owing to their high chemical stability. To study the applicability and validity of this sensor based on the BW technique, at first simple commercial bovine serum albumin biomolecules (BSA) were tested (a detailed description of the tests shown in Publication 1). Thereafter, human serum exosomes were considered as analytes samples. Indeed, our sensing method aims to distinguish among the serum exosomes insulated from inflammatory diseased and healthy persons (a detailed description of the tests illustrated in Publication 1).

As schematically shown in Figure 25b, when the p-polarized light passes through the sample with an incidence angle close to the Brewster angle at the BW, volume detection with high sensitivity can be achieved. In this regard, the BW technique based on reflection mode shows strong sensitivity through significant wavelength shift ( $\Delta\lambda$ )  $\approx$  232 nm at the Brewster angle, as seen in Figure 26a. In contrast, concerning the transmission mode,  $\Delta\lambda$  is negligible ( $\approx$  20nm), as seen in Figure 26b. It is worth mentioning that such considerable detectability is barely attainable via a transmission/extinction mode[41], [89], [90]. The reason behind that is that the sensor-based reflection/BW effect operates once the presence of any variation in molecular polarizability that enclosed the nanoclusters. Moreover, the sensor offers visual detectability where the human eye can differentiate between exosomes of healthy individuals and patients based on reflection mode rather than transmission mode, as shown in Figure 26c. The sensing analytical performance of the plasmonic BW sensor in the reflection and transmission modes based on changing the exosome’s concentration is illustrated in Figure 26d. It is noticed from the slope of fitted lines that the sensor based on Brewster dip (reflection mode) shows a strong sensitivity, compared to its sensitivity in the transmission mode.

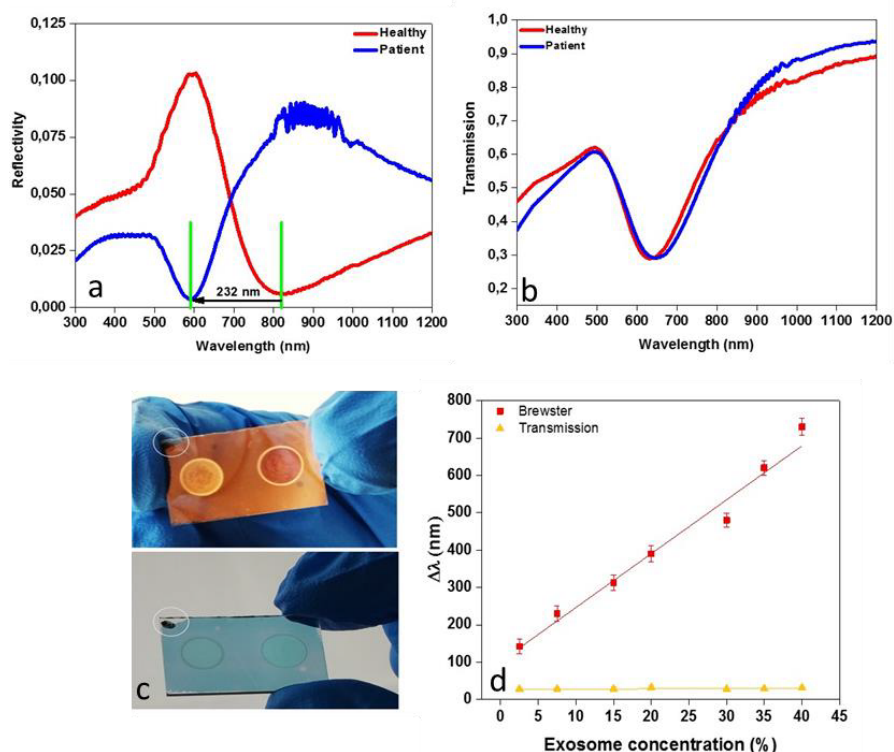


**Figure 26.** Naked-eye and bulk biodetection of analytes based on the polarizonic reflection and BW phenomenon of plasmonic dipoles. a) Reflectivity and b) transmission spectra of the Au nanoclusters platform covered with serum exosomes of inflammatory bowel patients (blue line) and healthy persons (red line). The specular reflection measurement was done at the Brewster angle ( $70^\circ$  angle of incidence). c) Camera image of the Au NPs on glass coated with the serum exosomes extracted from a diseased person with bowel inflammation (left) and a healthy person (right) in reflection and transmission states (top and bottom, respectively) (the circle mark at the top-left nook means the same biosensing platform is utilized but in various optical states). d) Linear fit for wavelength shifts ( $\Delta\lambda$ s) against the concentration of exosome under the BW effect and in transmission mode [Publication 1]. Reproduced with permission[64]. Copyright 2018, John Wiley and Sons.

Finally, based on this BW technique, the bulk biodetection can be achieved with a significant wavelength shift that is hardly attainable by plasmonic techniques based on transmission/extinction mode. Moreover, the sensor offers naked-eye detection. Concerning the fabrication method, a sputtering technique that is considered simple, cost-effective, and scalable was used. In contrast to the biodetection traditional technique, there is no need for sophisticated lithographic patterning or precise alignment of light coupling.





## 5. Conclusions

In this thesis, we focused on presenting the fascinating polarizonic concept of the oscillating disordered plasmonic nanodipoles that are well-known for their absorptivity for light. This emerging concept enables exploring some interesting properties not achievable via the plasmonic extinction of light. We showed the potential of such plasmonic metal dipoles in addition to the lossless oxide nanomaterials in being able to radiate vivid polarizonic structural reflective colors. These colors have been generated at the resonance frequencies even if the dipoles exist on a blackbody. Here, the polarizonic colors and their remarkable potential in a variety of advanced applications such as solar energy-saving and biosensing were highlighted. In this regard, we presented the perfect solar absorbers not only in a dark appearance but also in a vivid diverse coloration. To achieve that, metallic nanoclusters and transflective oxide nanoobjects have been utilized. Moreover, the plasmonic BW effect was utilized as a new platform for bulk biosensing with naked-eye detection of analytes. Concerning the production method, the plasmonic metal nanoobjects and the oxides metaparticles were synthesized by the sputtering technique and Leidenfrost green chemical reactor, respectively. Finally, the summary is divided into four parts to cover individually each of the applications as follows:

- a) **Tailored perfect colored absorber based on a blackbody:** Polarizonic reflection of Ag NPs/nanocomposite deposited on a black substrate were studied. In case of a change of deposited metal thickness, the reflective coloration has been easily tuned. Accordingly, the samples showed a distinctive radiative coloration and they concurrently have complete absorptivity. Also, silver NPs samples covered with a hybrid matrix at different thicknesses and different ratios were prepared. Based on the optical results of the samples, it has been found that the PRC offers higher environmental sensitivity. Moreover, the PRCs of the samples can be easily detected by the naked eye in reflection mode. As a result, a library of polarizonic structural coloration based-blackbody analogous to attractive rainbow colors was achieved. In conclusion, the presented method is considered as an innovative design for the fabrication of tailored perfect colored absorber “colored solar materials” in a simple, scalable, and cost-effective manner.
- b) **Solar aluminum kitchen foils with vivid colors:** A new generation of tailored perfect-colored absorbers that are omnidirectional was established through dipolar reflection and the interference mode, i.e., polarizonic interference-effect. Such effect was elucidated by depositing the

silver nanocomposite on a grey substrate such as aluminium kitchen foil, the coated foil appeared in a golden color, i.e., a gold-free golden foil. Since the reflection resonance of nanocomposite can be adjusted via the volume fraction and distribution of the embedded NPs and the dielectric constant of the host medium, significant numbers of composites can be accomplished. In this regard, ultrathin nanocomposites with different filling factors (20%, 25%, 32%, and 40% of Au) and various dielectric hosts (SiO<sub>2</sub>, TiO<sub>2</sub>, and (50/50) SiO<sub>2</sub>-TiO<sub>2</sub>) coated flexible Al foil substrates were fabricated. As a result, a colored double-layered perfect solar absorber can be simply reached based on the interference effect. Besides, the fabricated colored foils can be utilized for decoration and packaging purposes, among others. Finally, the use of such cheap and easily shapeable Al foils as a substrate permits the production of these solar materials in a scalable, economical manner.

- c) **Perfect black solar absorber:** The design of the thinnest black solar absorber (with intensity around 100% at the optical spectrum) based on ultrathin metacomposite was introduced. Such metacomposite is composed of transfective oxide (CuO) metaparticles immersed in a polymer medium. These metaparticles containing self-organized nanoconstituents were fabricated in the Leidenfrost green chemical reactor. Additionally, these oxide metaparticles were synthesized in different sizes and morphology, the rice-shaped metaparticles showed a PRC in contrast to star-like structures. Hence, in the presence of a broad reflector mirror and such rice-shaped metaparticles, the solar radiation at the visible frequencies can be captured through polarizonic interference-effect. As a result, the perfect solar absorber was fabricated of two layers: ultrathin rice-shaped metacomposite thin film and an underlying silver mirror. This perfect solar absorber works by exploiting the “distractive” polarizonic interference of these layers.
- d) **Naked-eye and bulk biodetection:** Based on the polarizonic reflection and BW effect of plasmonic metal NPs occurring at the LSPR, a new platform for the naked-eye and bulk biodetection of analytes was introduced. Indeed, bulk detection (i.e., bulk RI monitoring) acts as a big challenge for the conventional plasmon resonance technique. In contrast, the sensor-based polarizonic/BW effect operates once the existence any change in molecular polarizability that surrounded the NPs. In this respect, Au nanoclusters covered a substrate were used as a bio-sensor platform. Using the BW technique, the distinction between the serum exosomes insulated from inflammatory diseased and healthy persons was achieved. Additionally, The sensor platform based on polarizonic reflection enabled naked-eye recognition of the analytes. Finally, the sensing analytical performance of the BW sensor based on reflection mode showed a strong sensitivity. Whereas such high sensitivity could not be achieved in transmission/extinction mode.

## 6. Outlook

The specular reflected polarzonic coloration based on disordered nanodipoles/nanocomposite is novel and can be considered as an emerging field, where it holds a huge potential in many fields including energy saving and harvesting, decoration, and biosensing.

As a promising aspect from an unambiguous control of the resultant polarizonic reflection peak, the polarizonic concept can be implemented perfectly well in disordered bimetallic alloyed systems, as our preliminary experimental results showed. The bimetallic alloy systems allow precise tunability of the polarizonic reflective coloration through the manipulation of the alloy's compositional ratios, which leads to an alternation of the complex RI of the system resulting in distinct controllable polarizonic performance. We speculate that by using a wide range of metals and their alloys, a significant number of vividly colored surfaces can be attained, whereas combining this technology with a PVD roll-to-roll technique will facilitate industrial-scale manufacturing in a controlled, cheap, and versatile manner.

In terms of the future trend, we believe that the polarizonic concept can be extended to the Earth Abundant Metals such as iron, cobalt, nickel, magnesium, etc., which offer a polarizonic response, as a cheap and efficient alternative of noble metals for the production of large-scale colored surfaces. Such a tendency will be very promising towards achieving a sustainable future via functional and decorative applications.



# References

- [1] M. Song *et al.*, “Colors with plasmonic nanostructures: A full-spectrum review,” *Appl. Phys. Rev.*, vol. 6, no. 4, 2019.
- [2] I. Freestone, N. Meeks, M. Sax, and C. Higgitt, “The Lycurgus Cup - A Roman nanotechnology,” *Gold Bull.*, vol. 40, no. 4, pp. 270–277, 2008.
- [3] D. Barchiesi, “Lycurgus Cup: inverse problem using photographs for characterization of matter,” *J. Opt. Soc. Am. A*, vol. 32, no. 8, p. 1544, 2015.
- [4] H. Müller, “Optical Properties of Metal Clusters,” *Zeitschrift für Phys. Chemie*, vol. 194, no. Part 2, pp. 278–279, 1996.
- [5] C. Kittel and D. L. Dexter, “Introduction to Solid State Physics,” *Am. J. Phys.*, vol. 21, no. 8, pp. 650–650, 1953.
- [6] Y. Wang, G. J. Desroches, and R. J. Macfarlane, “Ordered polymer composite materials: Challenges and opportunities,” *Nanoscale*, vol. 13, no. 2, pp. 426–443, 2021.
- [7] M. Šupová, G. S. Martynková, and K. Barabaszová, “Effect of nanofillers dispersion in polymer matrices: A review,” *Sci. Adv. Mater.*, vol. 3, no. 1, pp. 1–25, 2011.
- [8] S. Homaeigohar and M. Elbahri, “Switchable Plasmonic Nanocomposites,” *Adv. Opt. Mater.*, vol. 7, no. 1, pp. 1–33, 2019.
- [9] P. K. Jain and M. A. El-Sayed, “Plasmonic coupling in noble metal nanostructures,” *Chem. Phys. Lett.*, vol. 487, no. 4–6, pp. 153–164, 2010.
- [10] M. I. Stockman, “Nanoplasmonics: The physics behind the applications,” *Phys. Today*, vol. 64, no. 2, pp. 39–44, 2011.
- [11] W. A. Murray and W. L. Barnes, “Plasmonic materials,” *Adv. Mater.*, vol. 19, no. 22, pp. 3771–3782, 2007.
- [12] H. Fröhlich, *Theory of dielectrics: Dielectric constant and dielectric loss*. Oxford : Clarendon, 1958.
- [13] M. Abdelaziz, S. Homaeigohar, M. K. Hedayati, M. A. Assad, and M. Elbahri, “Solar Aluminum Kitchen Foils with Omnidirectional Vivid Polarizonic Colors,” vol. 1900737, pp. 1–7, 2019.
- [14] N. Jiang, X. Zhuo, and J. Wang, “Active Plasmonics : Principles , Structures , and Applications,” 2018.
- [15] Mady Elbahri, M. K. Hedayati, S. Homaeigohar, and M. Abdelaziz, “Reawakening of Plasmonic Nanocomposites with Polarizonic Reflective Coloration: From Metal to Molecules,” in *Cluster Beam Deposition of Functional Nanomaterials and Devices*, 1st Editio., P. Milani and M. Sowwan, Eds. Elsevier, 2020, p. 354.
- [16] R. Ruppín, “Evaluation of extended Maxwell-Garnett theories,” *Opt. Commun.*, vol. 182, no. 4, pp. 273–279, 2000.
- [17] R. Del Coso, J. Requejo-Isidro, J. Solis, J. Gonzalo, and C. N. Afonso, “Third order nonlinear optical susceptibility of Cu:Al<sub>2</sub>O<sub>3</sub> nanocomposites: From spherical nanoparticles to the percolation threshold,” *J. Appl. Phys.*, vol. 95, no. 5, pp. 2755–2762, 2004.
- [18] P. Sciau, “Nanoparticles in Ancient Materials : The Metallic Lustre Decorations of Medieval Ceramics,” *InTeck*, no. May, 2012.
- [19] S. Kinoshita, S. Yoshioka, and J. Miyazaki, “Physics of structural colors,” vol. 076401, 2008.

- [20] B. Yang, H. Cheng, S. Chen, and J. Tian, "Structural colors in metasurfaces: principle, design and applications," *Mater. Chem. Front.*, vol. 3, no. 5, pp. 750–761, 2019.
- [21] J. Sun, B. Bhushan, and J. Tong, "Structural coloration in nature," *RSC Adv.*, vol. 3, no. 35, pp. 14862–14889, 2013.
- [22] L. Shang, Z. Gu, and Y. Zhao, "Structural color materials in evolution," *Mater. Today*, vol. 19, no. 8, pp. 420–421, 2016.
- [23] S. Kinoshita and S. Yoshioka, "Structural Colors in Nature: The Role of Regularity and Irregularity in the Structure," *ChemPhysChem*, vol. 6, no. 8, pp. 1442–1459, 2005.
- [24] T. S. Kustandi, H. Y. Low, J. H. Teng, I. Rodriguez, and R. Yin, "Mimicking domino-like photonic nanostructures on butterfly wings," *Small*, vol. 5, no. 5, pp. 574–578, 2009.
- [25] J. Huang, X. Wang, and Z. L. Wang, "Controlled replication of butterfly wings for achieving tunable photonic properties," *Nano Lett.*, vol. 6, no. 10, pp. 2325–2331, 2006.
- [26] T.-H. Wong, M. C. Gupta, B. Robins, and T. L. Levendusky, "Color generation in butterfly wings and fabrication of such structures," *Opt. Lett.*, vol. 28, no. 23, p. 2342, 2003.
- [27] C. Lawrence, P. Vukusic, and R. Sambles, "Grazing-incidence iridescence from a butterfly wing," *Appl. Opt.*, vol. 41, no. 3, p. 437, 2002.
- [28] M. Srinivasarao, "Nano-Optics in the Biological World: Beetles, Butterflies, Birds, and Moths," *Chem. Rev.*, vol. 99, no. 7, pp. 1935–1961, 1999.
- [29] H. Ghiradella, "Light and color on the wing: structural colors in butterflies and moths," *Appl. Opt.*, vol. 30, no. 24, p. 3492, 1991.
- [30] M. K. Hedayati, "Review of Metasurface Plasmonic Structural Color," pp. 1463–1479, 2017.
- [31] A. R. Parker, "Natural photonic engineers," *Mater. Today*, vol. 5, no. 9, pp. 26–31, 2002.
- [32] Y. Zhao, Z. Xie, H. Gu, C. Zhu, and Z. Gu, "Bio-inspired variable structural color materials," *Chem. Soc. Rev.*, vol. 41, no. 8, pp. 3297–3317, 2012.
- [33] A. Kristensen *et al.*, "Plasmonic colour generation," *Nat. Rev. Mater.*, vol. 2, no. 1, p. 16088, 2016.
- [34] R. O. Prum, R. L. Morrison, and G. R. Ten Eyck, "Structural color production by constructive reflection from ordered collagen arrays in a bird (*Philepitta castanea*: Eurylaimidae)," *J. Morphol.*, vol. 222, no. 1, pp. 61–72, 1994.
- [35] J. R. Mejía-Salazar and O. N. Oliveira, "Plasmonic Biosensing," *Chem. Rev.*, vol. 118, no. 20, pp. 10617–10625, 2018.
- [36] R. T. Hill, "Plasmonic Biosensors NIH Public Access," pp. 1–28, 2016.
- [37] S. Unser, I. Bruzas, J. He, and L. Sagle, "Localized Surface Plasmon Resonance Biosensing: Current Challenges and Approaches," pp. 15684–15716, 2015.
- [38] J. N. Anker, W. P. Hall, O. Lyandres, N. C. Shah, J. Zhao, and R. P. Van Duyne, "Biosensing with plasmonic nanosensors," no. June 2014, 2008.
- [39] M. Li, S. K. Cushing, and N. Wu, "Plasmon-enhanced optical sensors: a review," *Analyst*, vol. 140, no. 2, pp. 386–406, 2015.
- [40] C. Sönnichsen, B. M. Reinhard, J. Liphardt, and A. P. Alivisatos, "A molecular ruler based on plasmon coupling of single gold and silver nanoparticles," *Nat. Biotechnol.*, vol. 23, no. 6, pp. 741–745, 2005.
- [41] H. Im *et al.*, "Label-free detection and molecular profiling of exosomes with a nano-plasmonic sensor," *Nat. Biotechnol.*, vol. 32, no. 5, pp. 490–495, 2014.
- [42] G. L. Liu *et al.*, "A nanoplasmonic molecular ruler for measuring nuclease activity and DNA footprinting," *Nat. Nanotechnol.*, vol. 1, no. 1, pp. 47–52, 2006.
- [43] V. G. Kravets *et al.*, "Singular phase nano-optics in plasmonic metamaterials for label-free single-molecule detection," *Nat. Mater.*, vol. 12, no. 4, pp. 304–309, 2013.
- [44] M. K. Hedayati, F. Faupel, and M. Elbahri, "Review of Plasmonic Nanocomposite Metamaterial Absorber," pp. 1221–1248, 2014.
- [45] M. Elbahri *et al.*, "An omnidirectional transparent conducting-metal-based plasmonic nanocomposite," *Adv. Mater.*, vol. 23, no. 17, pp. 1993–1997, 2011.

- [46] M. K. Hedayati *et al.*, “Design of a perfect black absorber at visible frequencies using plasmonic metamaterials,” *Adv. Mater.*, vol. 23, no. 45, pp. 5410–5414, 2011.
- [47] H. Search, C. Journals, A. Contact, M. Iopscience, and I. P. Address, “Lithography-free broadband visible light absorber based on a mono-layer of gold nanoparticles,” vol. 025002.
- [48] C. Etrich, S. Fahr, M. K. Hedayati, F. Faupel, M. Elbahri, and C. Rockstuhl, “Effective optical properties of plasmonic nanocomposites,” *Materials (Basel)*, vol. 7, no. 2, pp. 727–741, 2014.
- [49] M. K. Hedayati, F. Faupel, and M. Elbahri, “Tunable broadband plasmonic perfect absorber at visible frequency,” *Appl. Phys. A Mater. Sci. Process.*, vol. 109, no. 4, pp. 769–773, 2012.
- [50] M. K. Hedayati, M. Abdelaziz, C. Etrich, S. Homaeigohar, C. Rockstuhl, and M. Elbahri, “Broadband anti-reflective coating based on plasmonic nanocomposite,” *Materials (Basel)*, vol. 9, no. 8, pp. 1–9, 2016.
- [51] M. K. Hedayati, A. U. Zillohu, T. Strunskus, F. Faupel, and M. Elbahri, “Plasmonic tunable metamaterial absorber as ultraviolet protection film,” *Appl. Phys. Lett.*, vol. 104, no. 4, 2014.
- [52] K. Aydin, V. E. Ferry, R. M. Briggs, and H. A. Atwater, “Broadband polarization-independent resonant light absorption using ultrathin plasmonic super absorbers,” pp. 1–7, 2011.
- [53] M. G. Nielsen, A. Pors, O. Albrechtsen, and S. I. Bozhevolnyi, “Efficient absorption of visible radiation by gap plasmon resonators,” vol. 20, no. 12, pp. 13311–13319, 2012.
- [54] C. Hägglund *et al.*, “Self-Assembly Based Plasmonic Arrays Tuned by Atomic Layer Deposition for Extreme Visible Light Absorption,” *Nano Lett.*, vol. 13, no. 7, pp. 3352–3357, Jul. 2013.
- [55] J. Hao *et al.*, “High performance optical absorber based on a plasmonic metamaterial,” vol. 251104, no. 2010, pp. 1–4, 2016.
- [56] N. Liu, M. Mesch, T. Weiss, M. Hentschel, and H. Giessen, “Infrared Perfect Absorber and Its Application As Plasmonic Sensor,” *Nano Lett.*, vol. 10, no. 7, pp. 2342–2348, Jul. 2010.
- [57] P. Nordlander and E. Prodan, “Plasmon Hybridization in Nanoparticles near Metallic Surfaces,” *Nano Lett.*, vol. 4, no. 11, pp. 2209–2213, Nov. 2004.
- [58] M.A. Biot, “Some new aspects of the reflection of electromagnetic waves on a rough surface,” *J. Appl. Phys.*, vol. 28, no. 12, pp. 1455–1463, 1957.
- [59] M. Elbahri *et al.*, “Photoswitchable molecular dipole antennas with tailored coherent coupling in glassy composite,” no. August 2014, pp. 1–8, 2015.
- [60] M. A. Assad, S. Homaeigohar, and M. Elbahri, “Reflective Coloration from Structural Plasmonic to Disordered Polarizonic,” *Adv. Photonics Res.*, vol. 2100009, p. 2100009, 2021.
- [61] M. A. Rahman, S. M. K. Vivek, S. H. Kim, and J. Y. Byun, “Applied Surface Science Polarizonic-interference colouration of stainless steel surfaces by Au-Al<sub>2</sub>O<sub>3</sub> nanocomposite thin film coating,” *Appl. Surf. Sci.*, no. October, p. 144428, 2019.
- [62] J. Kim, H. Oh, M. Seo, and M. Lee, “Generation of Reflection Colors from Metal-Insulator-Metal Cavity Structure Enabled by Thickness-Dependent Refractive Indices of Metal Thin Film,” *ACS Photonics*, vol. 6, no. 9, pp. 2342–2349, 2019.
- [63] V. Astapenko, *Polarization Bremsstrahlung on Atoms, Plasmas, Nanostructures and Solids*, 1st ed. Springer-Verlag Berlin Heidelberg, 2013.
- [64] M. Elbahri *et al.*, “Plasmonic Metaparticles on a Blackbody Create Vivid Reflective Colors for Naked-Eye Environmental and Clinical Biodetection,” vol. 1704442, pp. 1–10, 2018.
- [65] M. Abdelaziz *et al.*, “Transflective Mesoscopic Nanoparticles Synthesized in the Leidenfrost Droplet as Black Absorbers,” vol. 1801610, pp. 1–6, 2019.
- [66] M. V. U. Kreibig, “Optical Properties of Metal Clusters,” *Springer*, 2013.
- [67] V. S. K. Chakravadhanula *et al.*, “Equal intensity double plasmon resonance of bimetallic quasi-nanocomposites based on sandwich geometry,” *Nanotechnology*, vol. 19, no. 22, 2008.



- [68] K. Seshan, *Handbook of Thin Film Deposition Techniques Principles, Methods, Equipment and Applications, Second Editon.* 2002.
- [69] M. Abdelaziz, S. Homaeigohar, M. K. Hedayati, M. A. Assad, and M. Elbahri, "Solar Aluminum Kitchen Foils with Omnidirectional Vivid Polarizonic Colors," *Adv. Opt. Mater.*, vol. 7, no. 15, pp. 1–7, 2019.
- [70] G. Mul, A. Zwijnenburg, B. Van der Linden, M. Makkee, and J. A. Moulijn, "Stability and selectivity of Au/TiO<sub>2</sub> and Au/TiO<sub>2</sub>/SiO<sub>2</sub> catalysts in propene epoxidation: An in situ FT-IR study," *J. Catal.*, vol. 201, no. 1, pp. 128–137, 2001.
- [71] Z. Ma, S. Brown, J. Y. Howe, S. H. Overbury, and S. Dai, "Surface modification of Au/TiO<sub>2</sub> catalysts by SiO<sub>2</sub> via atomic layer deposition," *J. Phys. Chem. C*, vol. 112, no. 25, pp. 9448–9457, 2008.
- [72] S. W. Yu, H. B. Liao, W. J. Wen, and G. K. L. Wong, "Au/TiO<sub>2</sub>/SiO<sub>2</sub> sandwich multilayer composite films with large nonlinear optical susceptibility," *Opt. Mater. (Amst.)*, vol. 27, no. 8, pp. 1433–1437, 2005.
- [73] A. Anders, "High power impulse magnetron sputtering and related discharges: Scalable plasma sources for plasma-based ion implantation and deposition," *Surf. Coatings Technol.*, vol. 204, no. 18–19, pp. 2864–2868, 2010.
- [74] M. Elbahri *et al.*, "Underwater Leidenfrost nanochemistry for creation of size-tailored zinc peroxide cancer nanotherapeutics," *Nat. Commun.*, vol. 8, no. May, pp. 1–10, 2017.
- [75] R. Abdelaziz *et al.*, "Green chemistry and nanofabrication in a levitated Leidenfrost drop," *Nat. Commun.*, vol. 4, pp. 1–10, 2013.
- [76] M. Elbahri, D. Paretkar, K. Hirmas, S. Jebril, and R. Adelung, "Anti-lotus effect for nanostructuring at the leidenfrost temperature," *Adv. Mater.*, vol. 19, no. 9, pp. 1262–1266, 2007.
- [77] N. Sahu, B. Parija, and S. Panigrahi, "Fundamental understanding and modeling of spin coating process: A review," *Indian J. Phys.*, vol. 83, no. 4, pp. 493–502, 2009.
- [78] T. Manabe *et al.*, "Rectangular (1 cm × 12 cm) YBCO films prepared by MOD using spin-coating and wire-bar coating," *J. Phys. Conf. Ser.*, vol. 43, no. 1, pp. 366–368, 2006.
- [79] H. G. Schantz, "Electromagnetic energy around Hertzian dipoles," *IEEE antennas Propag. Mag.*, vol. 43, no. 2, p. 50, 2001.
- [80] J. D. Jackson, "Classical Electrodynamics Third Edition," *Am. J. Phys.*, vol. 67, p. 808, 1999.
- [81] Q. Hao *et al.*, "Aluminum plasmonic photocatalysis," *Sci. Rep.*, vol. 5, pp. 1–7, 2015.
- [82] M. H. Lee *et al.*, "Roll-to-roll anodization and etching of aluminum foils for high-throughput surface nanotexturing," *Nano Lett.*, vol. 11, no. 8, pp. 3425–3430, 2011.
- [83] M. A. P. T. K. Ghosh, *Energy Resources and Systems*, Vol. 2. Springer Science & Business Media, 2011.
- [84] S. I. J. J. Michael, "Performance analysis of a copper sheet laminated photovoltaic thermal collector using copper oxide - water nanofluid," *Sol. Energy*, vol. 119, pp. 439–451, 2015.
- [85] M. Shimizu, M. Suzuki, F. Iguchi, and H. Yugami, "High spectral selectivity for solar absorbers using a monolayer transparent conductive oxide coated on a metal substrate," *J. Appl. Phys.*, vol. 121, no. 18, 2017.
- [86] D. K. A.R. Halpern, Y. Chen, R.M. Corn, "Surface plasmon resonance phase imaging measurements of patterned monolayers and DNA adsorption onto microarrays," *Anal Chem*, vol. 83, no. 7, pp. 2801–2806, 2011.
- [87] J. Becker, A. Trügler, A. Jakab, U. Hohenester, and C. Sönnichsen, "The optimal aspect ratio of gold nanorods for plasmonic bio-sensing," *Plasmonics*, vol. 5, no. 2, pp. 161–167, 2010.
- [88] N. Liu, M. Mesch, T. Weiss, M. Hentschel, and H. Giessen, "Infrared perfect absorber and its application as plasmonic sensor," *Nano Lett.*, vol. 10, no. 7, pp. 2342–2348, 2010.
- [89] J. Rak, "Extracellular vesicles - biomarkers and effectors of the cellular interactome in cancer," *Front. Pharmacol.*, vol. 4 MAR, no. March, pp. 1–14,

- 2013.
- [90] S. A. Melo *et al.*, “Glypican-1 identifies cancer exosomes and detects early pancreatic cancer,” *Nature*, vol. 523, no. 7559, pp. 177–182, 2015.





ISBN 978-952-64-0595-7 (printed)

ISBN 978-952-64-0596-4 (pdf)

ISSN 1799-4934 (printed)

ISSN 1799-4942 (pdf)

**Aalto University**  
**School of Chemical Engineering**  
**Department of Chemistry and Materials Science**  
[www.aalto.fi](http://www.aalto.fi)

**BUSINESS +  
ECONOMY**

**ART +  
DESIGN +  
ARCHITECTURE**

**SCIENCE +  
TECHNOLOGY**

**CROSSOVER**

**DOCTORAL  
DISSERTATIONS**